

RESEARCH ARTICLE

10.1002/2017JD026461

Special Section:

Deep Convective Clouds and Chemistry 2012 Studies (DC3)

Key Points:

- Lightning data assimilation improves model simulations of storm location and vertical structure
- Rear inflow jets within mesoscale convective systems may weaken boundary layer trace gas vertical transport
- The tracer vertical transport is more controlled by the vertical gradient of mass flux than the vertical gradient of trace gas

Correspondence to:

Y. Li,
liyunyao@terpmail.umd.edu

Citation:

Li, Y., et al. (2017), Evaluation of deep convective transport in storms from different convective regimes during the DC3 field campaign using WRF-Chem with lightning data assimilation, *J. Geophys. Res. Atmos.*, 122, 7140–7163, doi:10.1002/2017JD026461.

Received 7 JAN 2017

Accepted 12 JUN 2017

Accepted article online 14 JUN 2017

Published online 6 JUL 2017

Evaluation of deep convective transport in storms from different convective regimes during the DC3 field campaign using WRF-Chem with lightning data assimilation

Yunyao Li¹ , Kenneth E. Pickering¹ , Dale J. Allen¹ , Mary C. Barth² , Megan M. Bela^{3,4} , Kristin A. Cummings¹ , Lawrence D. Carey⁵ , Retha M. Mecikalski⁵ , Alexandre O. Fierro^{6,7} , Teresa L. Campos² , Andrew J. Weinheimer² , Glenn S. Diskin⁸ , and Michael I. Biggerstaff⁹ 

¹Department of Atmospheric and Oceanic Science, University of Maryland, College Park, Maryland, USA, ²National Center for Atmospheric Research, Boulder, Colorado, USA, ³Department of Atmospheric and Oceanic Sciences, University of Colorado Boulder, Boulder, Colorado, USA, ⁴National Oceanic and Atmospheric Administration Earth System Research Laboratory, Boulder, Colorado, USA, ⁵Department of Atmospheric Science, University of Alabama in Huntsville, Huntsville, Alabama, USA, ⁶Cooperative Institute for Mesoscale Meteorological Studies, University of Oklahoma, Norman, Oklahoma, USA, ⁷National Severe Storms Laboratory, OAR, NOAA, Norman, Oklahoma, USA, ⁸NASA Langley Research Center, Hampton, Virginia, USA, ⁹School of Meteorology, University of Oklahoma, Norman, Oklahoma, USA

Abstract Deep convective transport of surface moisture and pollution from the planetary boundary layer to the upper troposphere and lower stratosphere affects the radiation budget and climate. This study analyzes the deep convective transport in three different convective regimes from the 2012 Deep Convective Clouds and Chemistry field campaign: 21 May Alabama air mass thunderstorms, 29 May Oklahoma supercell severe storm, and 11 June mesoscale convective system (MCS). Lightning data assimilation within the Weather Research and Forecasting (WRF) model coupled with chemistry (WRF-Chem) is utilized to improve the simulations of storm location, vertical structure, and chemical fields. Analysis of vertical flux divergence shows that deep convective transport in the 29 May supercell case is the strongest per unit area, while transport of boundary layer insoluble trace gases is relatively weak in the MCS and air mass cases. The weak deep convective transport in the strong MCS is unexpected and is caused by the injection into low levels of midlevel clean air by a strong rear inflow jet. In each system, the magnitude of tracer vertical transport is more closely related to the vertical distribution of mass flux density than the vertical distribution of trace gas mixing ratio. Finally, the net vertical transport is strongest in high composite reflectivity regions and dominated by upward transport.

1. Introduction

Deep convection is an important mechanism in the transport of planetary boundary layer (PBL) air into the upper troposphere (UT) and lower stratosphere (LS, UTLS) [Dickerson *et al.*, 1987]. It only takes a few minutes to about an hour to transport an air parcel from the surface to the UT [Skamarock *et al.*, 2000]. Measurements from field campaigns [Dickerson *et al.*, 1987; Pickering *et al.*, 1988, 1996, 2001; Scala *et al.*, 1990; Thompson *et al.*, 1994; Stenchikov *et al.*, 1996; Wang *et al.*, 1996; Jung *et al.*, 2005; Bertram *et al.*, 2007; Homeyer *et al.*, 2014; Apel *et al.*, 2015] and satellites [Setvák and Doswell III, 1991; Levizzani and Setvák, 1996; Halland *et al.*, 2009; Jensen *et al.*, 2015; Livesey *et al.*, 2013] have demonstrated that deep convective transport affects the moisture and the chemical composition of the UTLS.

Deep convective transport of moist and polluted PBL air into the UTLS has a significant impact on climate. The vertical transport of ozone (O_3) precursor gases substantially increases the production rate of O_3 in cloud outflow [Pickering *et al.*, 1990, 1992a, 1992b] that occurs in the upper troposphere where winds are stronger and O_3 has a longer lifetime and, thus, an expanded range of influence than in the PBL. As reported in *Intergovernmental Panel on Climate Change* [2013], tropospheric O_3 is the third most important greenhouse gas. Additionally, the injection of PBL moisture into the stratosphere enhances the concentration of water vapor in the LS [Homeyer *et al.*, 2014], which is one of the leading causes for LS water vapor variability. According to Solomon *et al.* [2010], stratospheric water vapor is a key driver for decadal global surface climate change. In addition, recent studies argue that deep convective transport affects the aerosol vertical distribution, which is an important component of aerosol radiative forcing.

The mechanism of deep convective transport is complex. The amount of PBL air transported to the UTLS through deep convection depends on various meteorological and chemical factors. During the Preliminary Regional Experiment for Stormscale Operational Meteorology Program-Central Phase project, increased carbon monoxide (CO) concentrations in the UT due to convective transport from the PBL were documented in the 13 and 15 June storms [Dickerson *et al.*, 1987; Pickering *et al.*, 1989]. Conversely, in the 17 June case, the CO mixing ratio in the UT outflow was similar to levels found in background air. This was hypothesized to possibly arise from the passage of a cold front, which prevented direct entry of PBL air into the cloud causing cloud inflow to be dominated by air from above the PBL [Pickering *et al.*, 1988]. Hence, large-scale conditions play an important role in deep convective transport.

Besides large-scale factors, PBL conditions and storm dynamics also affect deep convective transport. A model simulation of deep convective transport in a mesoscale convective complex observed during the North Dakota Thunderstorm Project in 1989 showed that a moister PBL produced stronger transport of CO from the PBL to the anvil region [Stenchikov *et al.*, 1996]. Several additional case studies have shown that deep convective transport is closely related to storm vertical velocity as well as storm propagation speed [Pickering *et al.*, 1992a; Wang *et al.*, 1996]. A recent study by Bigelbach *et al.* [2014] simulated the mass transport during the 2007 convective season in the U.S. Southern Great Plains. The results demonstrated that quasi-isolated strong convection exhibited stronger and deeper flux than mesoscale convective systems (MCSs), which indicated that the deep convective transport varied with different types of convective regimes.

The inflow structure also influences deep convective transport [Barth *et al.*, 2007]. Scala *et al.* [1990] used a two-dimensional moist cloud model to determine the transport pathways within a wet season continental tropical squall line observed during the National Aeronautics and Space Administration (NASA) Amazon Boundary Layer Experiment 2B field campaign. Parcel trajectory analysis illustrated that more than 50% of the air transported to the anvil region originated in the midtroposphere (at or above 6 km) rather than the PBL. More than 50% of PBL air entering the core updrafts terminated below 5 km and became involved in a rotor circulation at 4.5 km. Only about 15% of the PBL air was transported directly to the cloud top near 12 km. On the other hand, during the Amazon dry season, convective events over Brazilian biomass burning regions show substantial vertical transport of O₃ precursors to the UT leading to large O₃ production [Pickering *et al.*, 1991, 1992a, 1992c, 1992b, 1996]. Midlatitude studies have shown that most of the mass transport into the UTLS originated in the PBL [Skamarock *et al.*, 2000; Mullendore *et al.*, 2005].

Model simulations are often used to study deep convective transport [Barth *et al.*, 2007]. A reliable simulation of deep convective transport of trace gases remains challenging as it requires the model to faithfully reproduce large-scale conditions, PBL structure, storm evolution status, inflow structure, and the surrounding chemical composition. The Weather Research and Forecasting (WRF) model is a three-dimensional compressible non-hydrostatic atmospheric modeling system designed for both meteorological research and numerical weather prediction. WRF-Chem [Grell *et al.*, 2005; Fast *et al.*, 2006; Peckham *et al.*, 2011] is WRF coupled with atmospheric chemistry and simulates the emission, transport, mixing, and chemical transformation of trace gases and aerosols simultaneously with the meteorology. Recently, several studies have applied WRF and WRF-Chem to simulate convective transport from the PBL to the anvil region [e.g., Siu *et al.*, 2015; Bela *et al.*, 2016].

In this study WRF-Chem is employed to simulate storms of three different convective regimes that occurred during the Deep Convective Clouds and Chemistry (DC3) field campaign [Barth *et al.*, 2015]: an air mass thunderstorm, a severe supercell thunderstorm, and an MCS case. While this study focuses on the convective transport of CO and O₃, two trace gases with chemical lifetimes much longer than the lifetime of a convective storm, we choose to use WRF-Chem for the analysis to facilitate ongoing analyses of the impact of lightning NO_x production, wet scavenging, and aqueous chemistry on the distribution of species such as NO_x, HCHO, HNO₃, and O₃. Lightning data assimilation is used to improve the representation of the observed storms in terms of timing of convection initiation (CI), location, and vertical structure. Next, vertical flux divergence is calculated for each case to evaluate deep convective transport.

The purpose of this study is to examine the underlying causes behind the differences in deep convective transport of trace gases among different scale storms as a function of storm stage, reflectivity, and region (i.e., updraft or downdraft region) through the use of two passive gas tracers and an examination of mesoscale dynamics.

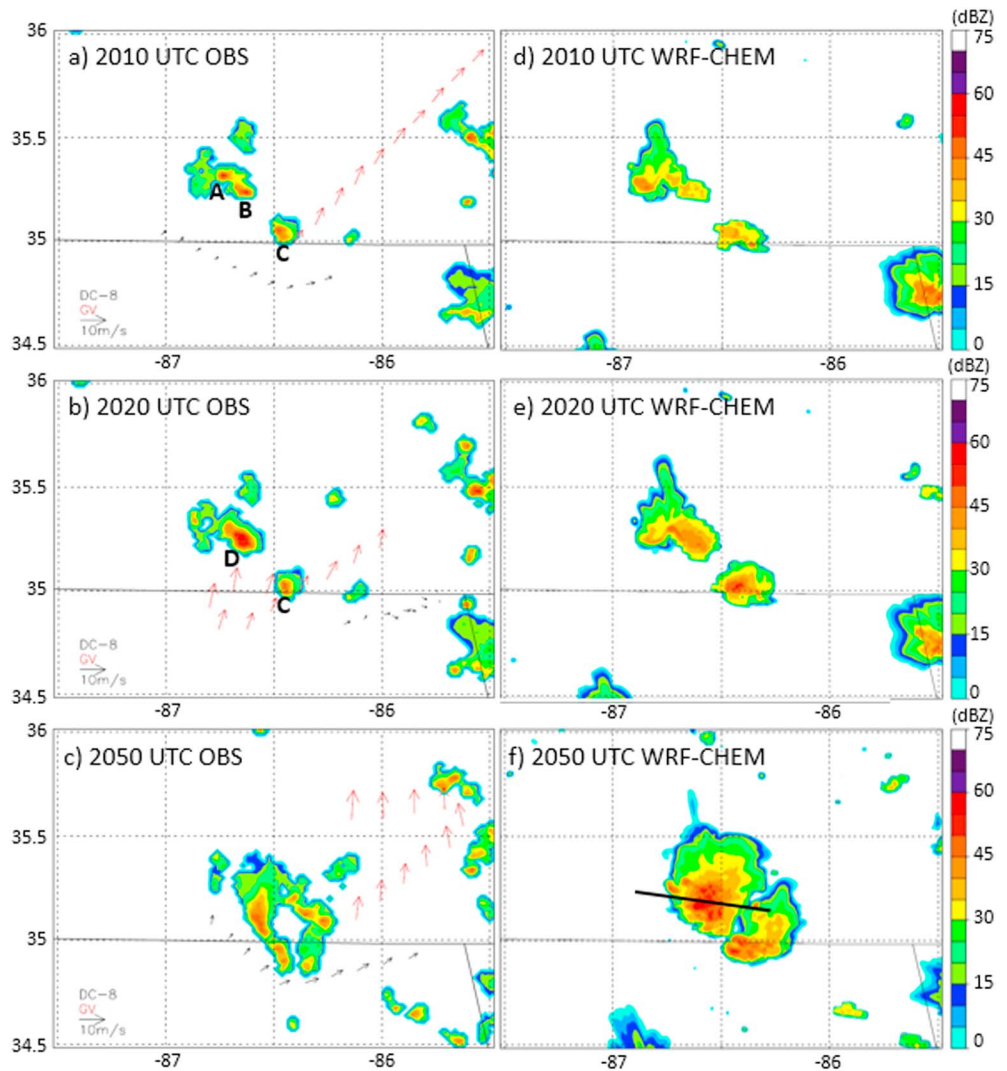


Figure 1. NEXRAD observed composite reflectivity (contours) with DC-8 (black arrows) and GV (red arrows) aircraft measured winds (storm motion removed) for the 21 May Alabama air mass storm case at (a) 2010 UTC, (b) 2020 UTC, and (c) 2050 UTC. Length of arrows corresponding to a 10 m s^{-1} wind is shown in the bottom left of each panel. The uppercase letters A–D refer to cells that are specifically discussed in the text. (d–f) WRF-Chem simulated composite reflectivity at the observation times. The black solid line in Figure 1f is the cross section line for Figures 7 and 13.

2. Observations and Methods

The Deep Convective Clouds and Chemistry (DC3) field campaign was conducted from 15 May through 30 June 2012 and sampled storms in three locations: (1) northeastern Colorado, (2) central Oklahoma to west Texas, and (3) northern Alabama. *Barth et al.* [2015] describe the full field experiment. The overarching purpose of the DC3 project was to examine the influence of midlatitude continental deep convective clouds on UT composition and chemistry.

2.1. Measurements

The field campaign made use of various types of measurements to characterize the dynamical, physical, chemical, and lightning processes during and after active convection. Three extensively instrumented aircraft platforms were utilized to gather in situ observations in the inflow and outflow regions of the convective storms: (1) the National Science Foundation (NSF)/National Center for Atmospheric Research (NCAR) Gulfstream-V (GV) aircraft, (2) the NASA DC-8 aircraft, and (3) the Deutsches Zentrum für Luft- und Raumfahrt Falcon aircraft. Only the GV and DC-8 aircraft data are used in this study [Chen et al., 2014a, 2014b, 2016a, 2016b]. Both aircraft

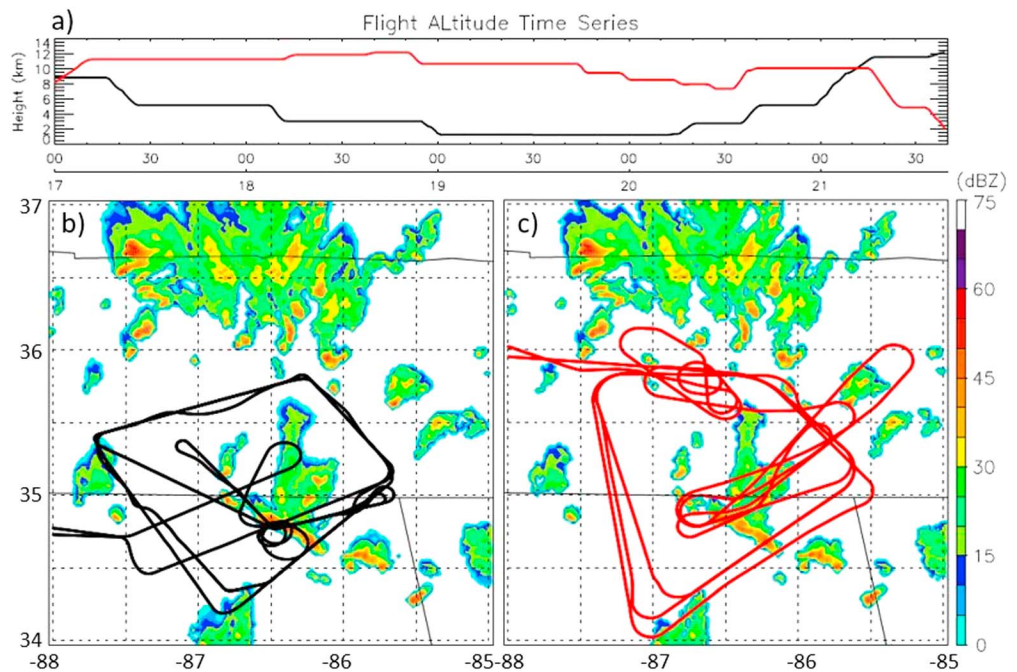


Figure 2. (a) 21 May Alabama air mass case DC-8 (black) and GV (red) flight altitude time series from 1700 to 2140 UTC. 21 May Alabama air mass case (b) DC-8 and (c) GV flight tracks superimposed on NEXRAD reflectivity at 2140 UTC.

measured a variety of gas phase species, aerosols, radiation, cloud particle characteristics, and meteorological properties. See Tables 2 and 3 in *Barth et al.* [2015] for the full GV and DC-8 payload, respectively.

The radar data used in this study are from the Next Generation Weather Radar (NEXRAD)-Weather Surveillance Radar-1988 Doppler (WSR-88D), with a horizontal resolution of 0.02° latitude and longitude, a vertical resolution of 1 km, and a temporal resolution of 5 min [*Homeyer et al.*, 2014]. Vertical velocity data for the 21 May Alabama case were derived from the WSR-88D and Advanced Radar for Meteorological and Operational Research (ARMOR) operated by the University of Alabama in Huntsville (UAH) [*Petersen et al.*, 2005; *Mecikalski et al.*, 2015]. For the Oklahoma case, Shared Mobile Atmospheric Research and Teaching (SMART) radar [*Biggerstaff et al.*, 2005; *Hill et al.*, 2013] and National Severe Storms Laboratory (NSSL) NOXP mobile radars were used to analyze storm vertical velocity.

The upper air data for the Alabama region are from UAH Mobile Radiosonde Observation Data (RAOB) and were provided by the University of Alabama-Huntsville. The upper air data for the Oklahoma region are from the NSSL, which deployed a Mobile GPS Advanced Upper-Air Sounding System. Routine upper air observations from the National Weather Service (NWS) are also used to provide information on the prestorm environment, as well as atmospheric conditions outside of mobile sounding regions.

Lightning data are used to improve model simulations and examine the ability of the model to predict lightning flash rates. The data come from two sources: (1) the Earth Networks Total Lightning Network (ENTLN) and (2) Lightning Mapping Array (LMA) in the North Alabama (NALMA) region [*Mecikalski et al.*, 2015]. Both ENTLN and LMA detect radio emissions (sferics) from cloud-to-ground and intracloud flashes.

2.2. Case Studies

For this research, we focus on the analysis of deep convective transport in convective systems of three different convective regimes from the DC3 campaign: (1) an air mass thunderstorm that occurred in northern Alabama on 21 May [*Mecikalski et al.*, 2015], (2) a supercellular storm system that initiated in Oklahoma on 29 May [*Bela et al.*, 2016], and (3) a linear MCS that took place in the central United States (over Missouri, Arkansas, and Illinois) on 11 June. There is a large degree of uncertainty concerning the relative frequency of each of these types of convection. *Doswell III* [2001] indicated that linear organization is the most common form of deep moist convective organization and that supercells are relatively rare events with the ratio of supercells to nonsupercells perhaps ~ 0.1 .

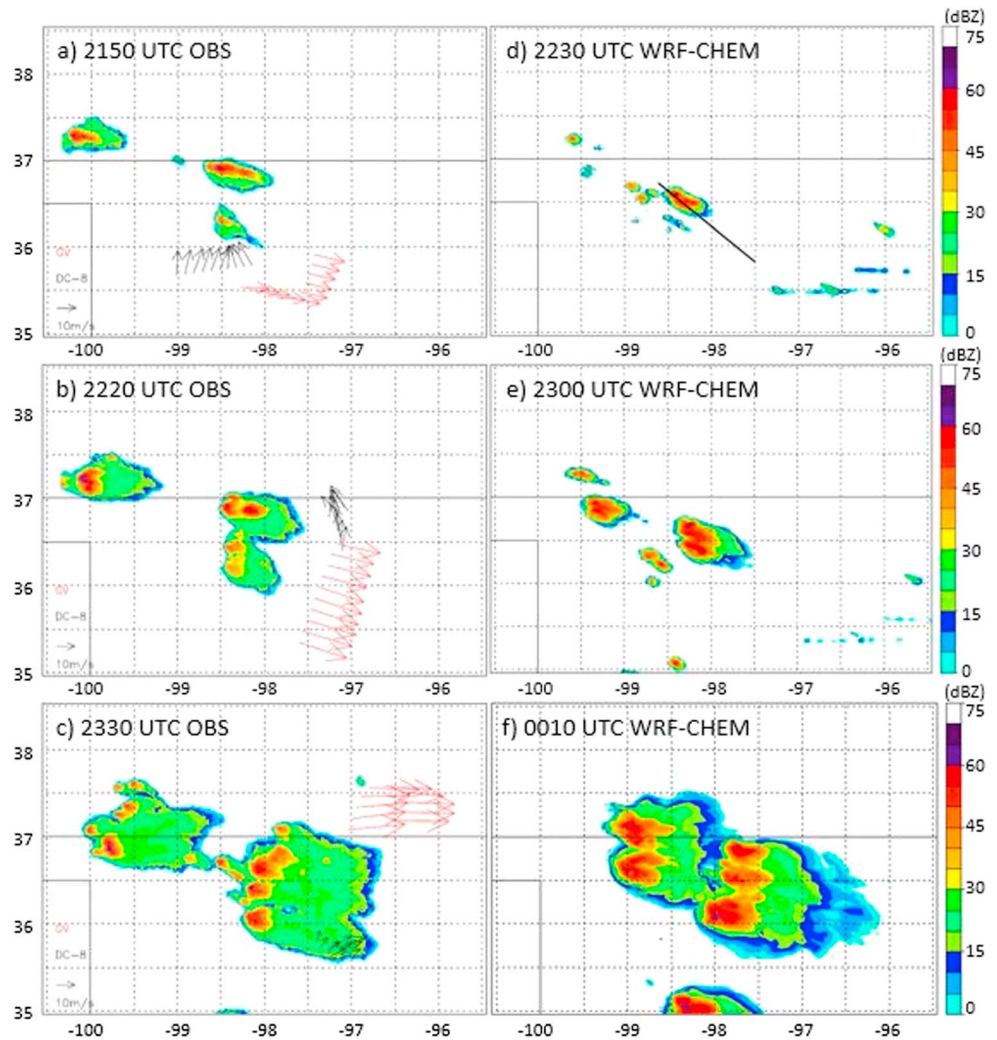


Figure 3. Similar to Figure 1 but for the 29 May Oklahoma supercell case at (a and d) 2150 UTC, (b and e) 2220 UTC, and (c and f) 2330 UTC. The black solid line in Figure 3d is the cross section line for Figure 14.

2.2.1. 21 May Alabama Air Mass Thunderstorm

On 21 May, several deep moist convective storms developed in south central Tennessee and northern central Alabama well ahead of a weak cold front [Mecikalski et al., 2015]. Our storm of interest (updraft A in Figure 1a) started around 1930 UTC in south central Tennessee. Later, at about 2000 UTC, another updraft (B) formed to the southeast of updraft A. Two distinct maxima in the NEXRAD radar composite reflectivity fields were observed (Figure 1). Meanwhile, an isolated cell (updraft/cell C in Figure 1a) developed to the south of the main cell near the Tennessee-Alabama border at approximately 1950 UTC. The two northern updrafts (A and B) merged around 2015 UTC, which produced an intensified updraft region (D) (Figure 1b) with a maximum upward vertical velocity of $\sim 12 \text{ m s}^{-1}$ by 2030 UTC. After 2030 UTC, weak environmental wind shear and a relatively strong cold pool caused an outflow boundary to propagate ahead of the main line of convection. Thus, the vertical motion in the northern cell weakened rapidly, and the storm started to decay. At ~ 2050 UTC, cell D merged with cell C to form a convective ring (Figure 1c). Finally, at the end of the sampling period, widespread multicell convection associated with the gust front organized along a broken line (Figure 2) and moved at $\sim 5 \text{ m s}^{-1}$ toward the southeast.

The DC-8 and GV aircraft took off at 1600 UTC. Both aircraft approached the study region before CI (i.e., before the composite radar reflectivity of the storm exceeded 20 dBZ). The two aircraft began conducting a trapezoid pattern over the Alabama ground radar and LMA coverage region to measure the chemistry composition at various altitudes in the prestorm environment. The GV flew clockwise above 10.5 km, while

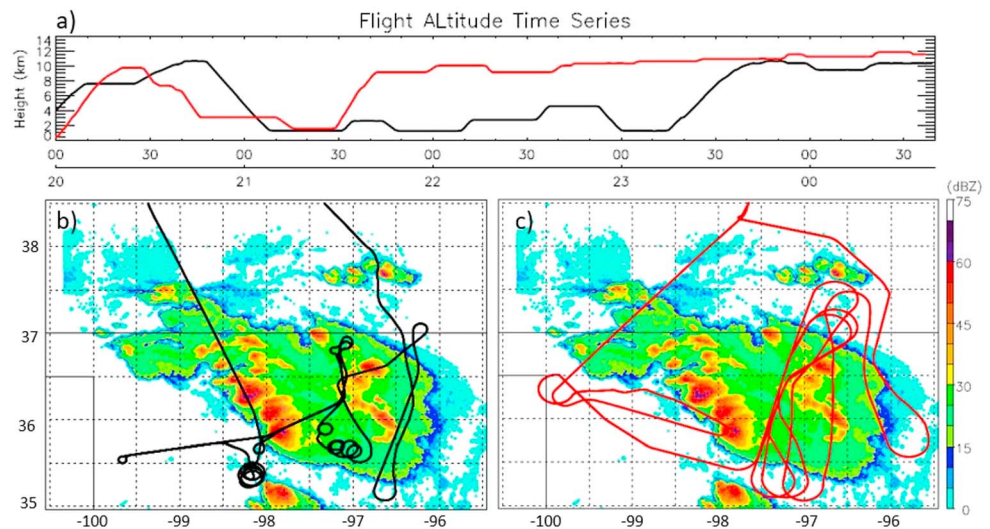


Figure 4. (a) 29 May Oklahoma supercell case DC-8 (black) and GV (red) flight altitude time series from 2000 to 0040 UTC. The 29 May Oklahoma supercell case (b) DC-8 and (c) GV flight tracks superimposed on NEXRAD reflectivity at 0040 UTC.

the DC-8 flew counterclockwise at 5 km, 3 km, and 1 km (Figure 2). At 1940 UTC, the GV moved toward the storm and sampled at several levels above 8 km. At 2040 UTC, the GV flew out of the storm to take measurements at ~ 10 km in the outflow region to the north of storm and then descended to 1 km. Meanwhile, the DC-8 flew from northwest to southeast of the convection in the inflow region at altitudes of 1 km, 3 km, and 5 km. Then the DC-8 spiraled up and passed across the top of the storm before returning to base. Four sounding balloons were launched during this mission. Two were released before CI at 1528 UTC and 1751 UTC, while the other two were launched after cells were formed at 2037 UTC [Mecikalski *et al.*, 2015, Figure 4] and 2215 UTC. The CAPE (785 J kg^{-1}) was relatively modest, which hampered the development of appreciable vertical velocities. The ARMOR Doppler velocity data indicated that the maximum vertical velocity over the entire system was only 13.9 m s^{-1} , which was much smaller than the two other storm cases described below.

2.2.2. 29 May Oklahoma Supercell Storm System

On 29 May, a thunderstorm system developed on the Oklahoma/Kansas border, around 2110 UTC, to the south of a quasi-stationary front near the Oklahoma and Kansas border. Two isolated cells initiated in the region of interest over northern Oklahoma. Both cells developed several updraft cores. At 2150 UTC, the northern cell was stronger than the southern cell with maximum reflectivity exceeding 60 dBZ (Figure 3a). Ten minutes later, both storms had midlevel mesocyclones [DiGangi *et al.*, 2016], marking the beginning of their supercellular stage. Around 2220 UTC, the southern cell split with the left mover merging into new convection to the north (Figure 3c). After the merger, the cells continued to strengthen, eventually producing a line of four supercells by 2300 UTC. Additional cells developed both west and east of the line of supercells, with the eastern cells forming a multicell band underneath the anvil of the southern supercell. The supercell complex intercepted a left-moving supercell from the south, which caused the southern supercell in the line to weaken. New supercells developed to the southwest of that merger. By 0300 UTC, the cloud system had evolved into a mostly multicell mesoscaleconvective system which propagated through central Oklahoma by 0400 on 30 May.

The SMART and NOXP radars sampled the two southernmost supercells in the line from about 2350 UTC on 29 May to 0000 UTC on 30 May. During the sampling time period, the Doppler-derived vertical motion in the southern supercell was sustained at greater than 35 m s^{-1} with several updraft pulses greater than 45 m s^{-1} . The strongest updraft, of about 65 m s^{-1} , was observed at 2330 UTC [DiGangi *et al.*, 2016, Figure 11]. The movement of the storm system was approximately 8.5 m s^{-1} toward the southeast.

Prior to the CI, the DC-8 flew down to an altitude of 1 km south of an area of cloud development to take inflow measurements and the GV flew at the same altitude in the western portion of this cloudy region. After convection initiated, the GV ramped up and set up a high-altitude wall to the east of the outflow. The

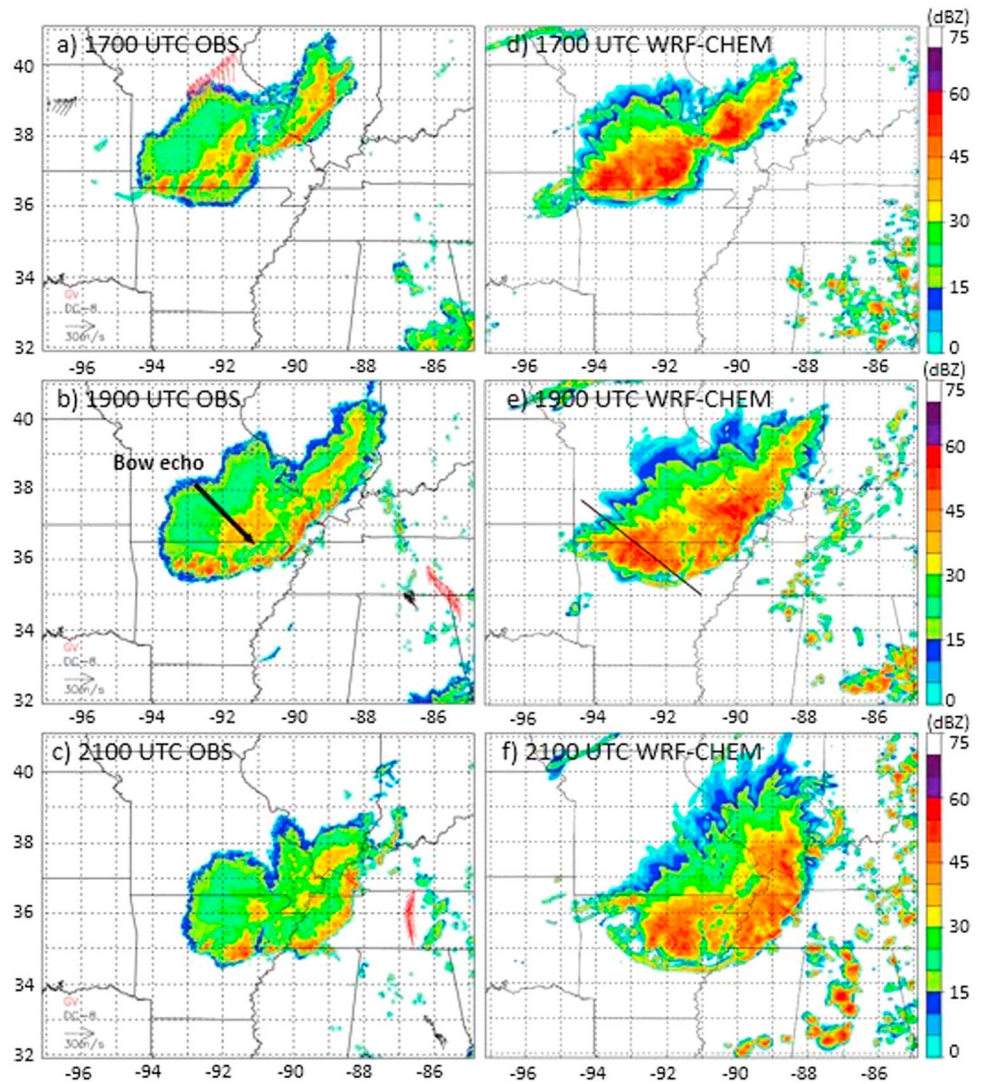


Figure 5. Similar to Figure 1 but for the 11 June central U.S. MCS case at (a and d) 1700 UTC, (b and e) 1900 UTC, and (c and f) 2100 UTC. The black solid line in Figure 5e is the cross section line for Figure 15.

convection and outflow moved toward the GV. Meanwhile, the DC-8 focused on gathering data in the low-level inflow region at altitudes of 1 km, 3 km, and 4.2 km to the east and southeast of the two convective cells. At ~2330 UTC, the DC-8 spiraled up and joined the GV to sample the outflow on the eastern edge of the storm (Figure 4). Three NSSL soundings were launched in the storm region. One was launched before storm initiation at 2029 UTC (CAPE was 3114 J kg^{-1}) [Bela *et al.*, 2016]. The other two were launched after the storm developed at 2255 UTC on 29 May and 0020 UTC on 30 May. The mixed-layer CAPE values at these two times were both quite large: 2562 J kg^{-1} and 3154 J kg^{-1} [DiGangi *et al.*, 2016]. The 0–6 km shear was about 24 m s^{-1} .

2.2.3. 11 June Central United States Mesoscale Convection System

This convective system initiated around 1900 UTC on 10 June. Several strong to severe thunderstorms developed along a line ahead of a sharp cold front that swept across Minnesota, North Dakota, South Dakota, and Nebraska. The main line of storms moved slowly to the east. At around 0530 UTC on 11 June, the main convective line broke into two parts. The northern storm system began to decay, while the southern part that extended from Wisconsin across Iowa to Kansas gained more strength and started to move southeastward. This MCS was located in the Illinois-Missouri-Arkansas region when sampling started at 1600 UTC (Figure 5) and moved southeast at a speed of 16 m s^{-1} reaching the Kentucky and Tennessee region by 2300 UTC. During the aircraft sampling, the MCS maintained its strength. This was the largest convective system

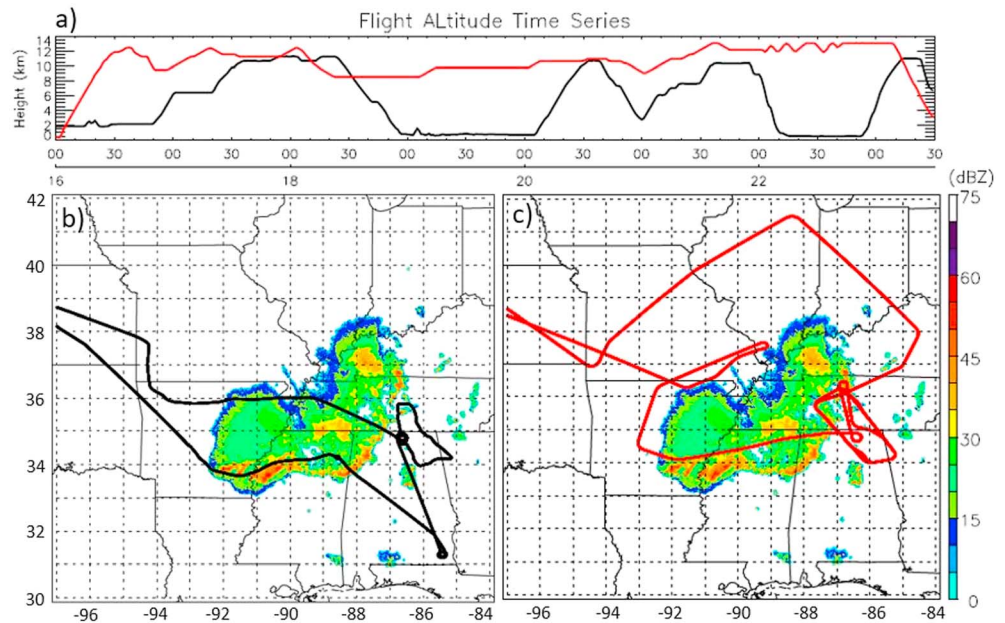


Figure 6. (a) 11 June central U.S. MCS case DC-8 (black) and GV (red) flight altitude time series from 1600 to 2230 UTC. 11 June central U.S. MCS case (b) DC-8 and (c) GV flight tracks superimposed on NEXRAD reflectivity at 2230 UTC.

considered in this analysis. The 1200 UTC surface CAPE reached 1147 J kg^{-1} at the Springfield, MO 88-D radar site (KSGF), and 2980 J kg^{-1} at the Little Rock 88-D radar site (KLZK).

The GV took off at 1600 UTC (Figure 6) and flew behind the line of convection to measure the outflow produced by the MCS. After 1800 UTC, the GV flew south to Alabama to perform additional sampling there. At 2120 UTC, the GV returned to the northern side of the still active MCS and sampled the outflow region before returning to base. The DC-8 took off at 1557 UTC and reached the MCS at 1700 UTC. The DC-8 flew around the south of the MCS and left for the Alabama region at 1800 UTC. After finishing sampling in the Alabama region, the DC-8 returned to the southern edge of the MCS at 2200 UTC. It made a rapid descent to 0.6 km to take measurements in the inflow region of the MCS.

3. Model Setup

In this research, the three-dimensional compressible nonhydrostatic Weather Research and Forecasting model with Chemistry (WRF-Chem) and the Advanced Research WRF dynamical core [Skamarock and Klemp, 2008] was utilized to simulate the aforementioned three case studies. Model output at 10 min intervals was used for the analysis. Sections 3.1 and 3.2 depict the model meteorology and chemistry setup for the three cases discussed above.

3.1. Meteorological Setup

For the 21 May Alabama air mass thunderstorm, the simulations (Table 1) were initialized on 21 May 2012 at 1500 UTC using meteorological initial conditions (IC) and boundary conditions (BC) derived from Global Forecast System (GFS) analysis with a 3 hourly time resolution. The WRF-Chem model simulation was conducted on three domains at cloud-parameterizing scale (15 km horizontal grid) and cloud-resolving scales (3 km and 0.6 km horizontal grids). There were 40 vertical levels with a 70 hPa model top. The time steps for each domain were 75 s, 15 s, and 3 s, respectively. The main physics choices were the WRF Single-Moment 6-class scheme (WSM6) [Hong and Lim, 2006] for microphysical processes, the Grell 3D cumulus parameterization [Grell, 1993; Grell and Devenyi, 2002] with shallow convection activated for the outermost domain, the Rapid Radiative Transfer Model for General Circulation Models (RRTMG) scheme [Iacono et al., 2008] for longwave radiation and shortwave radiation, the Noah scheme [Koren et al., 1999;

Table 1. WRF-Chem-LDA Model Configuration and Physics and Chemistry Options for All the Three Cases Analyzed in This Study, Which Are Listed on the Top Row

	21 May Air Mass	29 May Supercell	11 June MCS
Meteorology initial/boundary conditions	<i>GFS 15 UTC</i>	<i>NAM 18 UTC</i>	<i>NAM ANL 12 UTC</i>
Chemistry initial/boundary conditions	<i>DC-8 measurement to generate I.C. and B.C.</i>	<i>DC-8 measurement to generate I.C. and B.C.</i>	<i>MOZART</i>
Lightning data assimilation	<i>NALMA</i>	<i>ENTLN</i>	<i>ENTLN</i>
Grid resolution	<i>15 km, 3 km, 0.6 km</i>	<i>1 km</i>	<i>3 km</i>
Vertical levels	<i>40</i>	<i>89</i>	<i>40</i>
Time step	<i>75 s, 15 s, 3 s</i>	<i>3 s</i>	<i>15 s</i>
Cumulus parameterization	<i>Grell 3-D (in 15 km domain only)</i>	<i>no</i>	<i>no</i>
Microphysics	<i>WSM6</i>	<i>Morrison</i>	<i>WSM6</i>
PBL	<i>YSU</i>	<i>YSU</i>	<i>QNSE</i>
Longwave radiation		<i>RRTMG Scheme for all cases</i>	
Shortwave radiation		<i>RRTMG Scheme for all cases</i>	
Lightning schemes	<i>Price and Rind [1992; PR92] lightning flash rate scheme based on maximum vertical velocity for all cases</i>		
LNO _x scheme	<i>DeCaria et al. [2005] NO_x production as implemented by Barth et al. [2012] for all cases</i>		
Fire emissions	<i>FINN for all cases</i>		
Anthropogenic emissions	<i>NEI for all cases</i>		
Biogenic emissions	<i>MEGAN v2.04 for all cases</i>		
Chemistry option	<i>MOZCART for all cases</i>		

Tewari et al., 2004] for land surface processes, and the Yonsei University scheme (YSU) [*Hong et al., 2006*] for PBL mixing.

For the 29 May Oklahoma severe supercell case, the simulations of *Bela et al. [2016]* were analyzed. Their simulation of the storm was initialized on 29 May at 1800 UTC with meteorological IC and BC obtained from the 6 hourly 12 km North American Mesoscale Analysis (NAM-ANL). The WRF model simulations were conducted on a 1 km resolution domain with a time step of 3 s and 89 vertical levels. The main physics choices were the two-moment Morrison microphysics [*Morrison et al., 2009*], the RRTMG scheme for longwave and shortwave radiation, the Noah scheme for land surface, and YSU for PBL mixing.

For the 11 June central U.S. MCS case (Table 1), the model initiation time was on 11 June 2012 at 1200 UTC. Meteorological IC and BC were derived from the 3 hourly 12 km NAM-ANL. The model simulation was conducted on a 3 km resolution domain with 40 vertical levels and a model top of 70 hPa. The time step for this domain was 15 s. The main physics choices were WSM6 for microphysics, RRTMG for longwave and shortwave radiation, Noah scheme for land surface processes, and the Quasi-Normal Scale Elimination (QNSE) scheme [*Sukoriansky et al., 2005*] for PBL mixing.

We tried numerous different combinations of IC/BC conditions, WRF-Chem starting time, PBL schemes, and microphysics schemes in order to obtain the best possible simulation of the inflow, outflow, and vertical transport for each storm. The model setups listed above produced the best representation of each storm. When using NAM-ANL analyses to create the IC/BC, the simulation for the 21 May case resulted in too much precipitation. Thus, for this case, we use GFS to create the IC/BC instead. When evaluating different microphysics schemes coupled with Lightning Data Assimilation (LDA, more details about LDA are shown in section 3.3), it was found that employing the LDA together with the Morrison scheme generated a bounded weak echo region which is suitable for the supercell case but not for the other cases. Using different setups for each of the three cases aids in improving the simulations of the different convective regimes and thus allows us to better discuss and document the differences in the transport of insoluble trace gases among the different cases.

3.2. Chemistry Setup

For the 21 May air mass and 29 May supercell cases, the DC-8 and GV measured trace gas mixing ratios before convection initiated. Thus, we used these aircraft measurements to generate the chemical IC and BC within the aircraft sampling altitude range. Above the aircraft sampling altitude range, output from the Model for Ozone and Related chemical Tracers, version 4 (MOZART-4) was used to generate the IC and BC. Below the aircraft sampling range, a constant value of the lowest aircraft observation was used down to the surface. For the 11 June MCS case, no observations were available prior to CI over the region of interest. Therefore, we used MOZART-4 to create the entire chemical IC and BC (Table 1). Fire emissions were calculated from the Fire Inventory of NCAR (FINN) data [*Wiedinmyer et al., 2011*]. The 2011 National

Emissions Inventory (NEI) data were used to create anthropogenic emissions, and we used the Model of Emissions of Gases and Aerosols from Nature v2.04 (MEGAN) [Guenther *et al.*, 2006; Sakulyanontvittaya *et al.*, 2008] to generate biogenic emissions. Aircraft emission data were obtained from *Baughcum et al.* [1999].

The chemistry option selected for this work was the Model for Ozone and Related chemical Tracers (MOZART) gas phase chemistry [Emmons *et al.*, 2010] and Goddard Chemistry Aerosol Radiation and Transport aerosols [Chin *et al.*, 2002] (MOZCART) using the Kinetic Pre-Processor library. Photolysis rates were calculated using the Madronich Fast-Tropospheric Ultraviolet-Visible photolysis scheme [Tie *et al.*, 2003]. In addition, lightning flash rate and lightning NO_x (LNO_x) parameterizations were activated (see Table 1).

3.3. Lightning Data Assimilation

A lightning data assimilation (LDA) technique was employed to improve the WRF meteorological simulations. Based on *Fierro et al.* [2012, 2014, 2015], the following nudging equation was applied at observed lightning locations (i.e., grid columns) to locally increase the water vapor mass mixing ratio near or above its saturation value (with respect to liquid) in a confined layer within these columns:

$$Q_v = A Q_{\text{sat}} + B Q_{\text{sat}} \tanh(CX) \left[1 - \tanh\left(DQ_g^\alpha\right) \right] \quad (1)$$

The injection of water vapor mass (Q_v) increases the local perturbation virtual potential temperature, which increases the buoyancy accelerations and, ultimately, leads to the development of convection. In the simulations of the 21 May and 11 June cases, the values of the LDA coefficients were set to $A = 0.93$, $B = 0.2$, $D = 0.25$, and $\alpha = 2.2$. Some modifications were made to the *Fierro et al.* [2012] LDA scheme to improve the representation of the convective three-dimensional kinematical structure. First, the coefficient $A = 0.81$ in *Fierro et al.* [2012] was increased to 0.93 similar to *Fierro et al.* [2014, 2015] to increase the grid volume where Q_v is adjusted. In the *Fierro et al.* studies the Q_v increase was confined at midlevels within the graupel-rich, mixed phase region between 253 K and 273 K. In this study, however, Q_v was increased over a slightly deeper layer rooted at lower levels, namely, between 285 K and 261 K. These isotherms correspond, respectively, to the lifted condensation level and the level of maximum vertical velocity. This change was motivated by the findings of *Marchand and Fuelberg* [2014] and *Fierro et al.* [2016], which suggest that increasing Q_v in the lower troposphere (below 700 hPa) instead of the mixed-phase region allows convection to become more quickly rooted in the PBL and, in turn, better represents weakly forced moist convection. The value of C is based on the gridded number of flashes. In the original nudging equation, the product of C and total flashes controls the shape of the hyperbolic tangent function. We chose a different value of C for the 21 May case, because a different lightning data source was used for that case study. For the 21 May Alabama case, the North Alabama Lightning Mapping Array (NALMA) very high frequency (VHF) source data were employed, because of its ability to better depict the location of the storms cores. By virtue of their different range of frequency detection, the number of NALMA source data are, by design, larger than the number of ENTLN stroke data at a given point. Thus, the value of C had to be scaled accordingly. The 11 June case did not have VHF measurements; therefore, the ENTLN data were used instead.

The aforelisted changes in the coefficients of the LDA scheme of *Fierro et al.* [2012] helped WRF-Chem reproduce a better vertical velocity structure (Figure 7). For the 21 May case, a damping option was also added in the LDA scheme to suppress peripheral spurious convection. Specifically, during the 3 h period prior to CI, the relative humidity was reduced to 75% throughout the domain within the layer that extended from the LCL to 6 km altitude.

4. Model Simulation Results

NEXRAD composite reflectivity fields for the 21 May storms are evaluated against the WRF simulations with and without LDA in Figure 8. The model failed to simulate the storm without the help of LDA. Figure 1 shows the evolution of the 21 May storm in WRF-Chem with LDA. Figure 5 compares NEXRAD composite reflectivity with the WRF-Chem LDA simulation for 11 June. Without LDA, the MCS begins to dissipate during the aircraft measurement time period. With the aid of LDA, the simulated MCS develops along the observed storm track and maintains its strength. For the 29 May case, the storm location, size, and structure (intensity, anvil height, and extent) are well represented by the model with LDA compared to NEXRAD (Figure 3), but CI in the model occurs approximately 40 min later than was observed [Bela *et al.*, 2016]. The simulated chemistry fields are

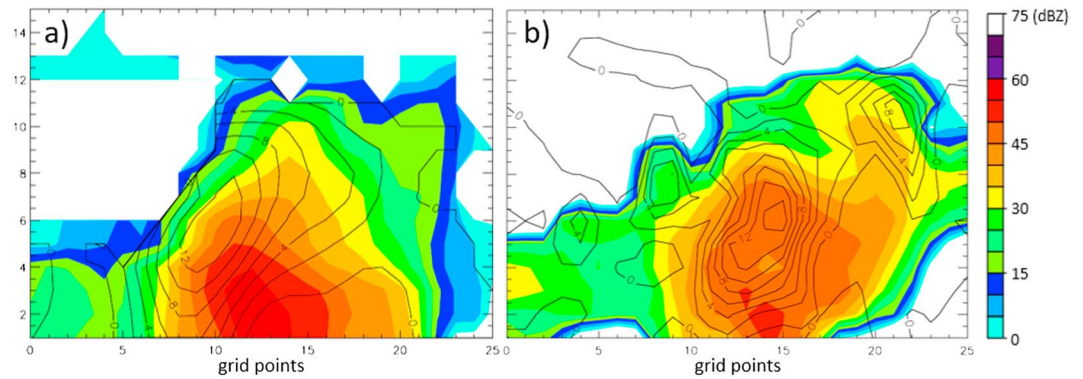


Figure 7. 21 May 2030 UTC (a) ARMOR observed and (b) WRF-Chem-LDA simulated vertical cross sections in the x - z plane along the black solid line highlighted in Figure 1f. The shadings represent the reflectivity fields in dBZ, and the black contours show the vertical motion. The distance between two grid points is 1 km.

reasonably consistent with observations for the three cases. In this study, CO was chosen as an example tracer to study the vertical transport because its source is primarily in the PBL. The WRF-Chem-LDA-simulated low-level inflow and high-level outflow CO and O₃ mixing ratios are evaluated against aircraft measurements for each case (Table 2). Model simulated CO mixing ratio in low-level inflow was within 5% of the aircraft measurements in all three cases. Simulated CO in the outflow region of the 29 May and 11 June cases were remarkably well reproduced by the model. For 21 May, however, the model underestimated CO by ~6%. The error for ozone in the storm outflow ranged from -9% to +6% over the three cases. The time periods of aircraft inflow and outflow measurements are based on Table 3 of *Fried et al.* [2016]. Moreover, the difference between the upper level CO mixing ratio in the storm affected region (polluted air) and unaffected region (background clean air) is frequently used to evaluate the overall strength of a storm. Therefore, the good comparison of observed and simulated CO mixing ratio (Table 2) provides compelling evidence that the transport in our simulations is reliable.

5. Deep Convection Vertical Transport Calculation

5.1. Vertical Flux Divergence

Deep convective transport was computed following *Skamarock et al.* [2000]. The conservation equation for a passive tracer species can be expressed as

$$\frac{\partial(\bar{\rho}\phi)}{\partial t} = -\frac{\partial(\bar{\rho}u\phi)}{\partial x} - \frac{\partial(\bar{\rho}v\phi)}{\partial y} - \frac{\partial(\bar{\rho}w\phi)}{\partial z} \quad (2)$$

where ϕ is the mixing ratio of the tracer, $\bar{\rho}$ is the mean air density, u and v are horizontal velocities, and w is vertical velocity. Integrating this equation in the horizontal over the domain yields

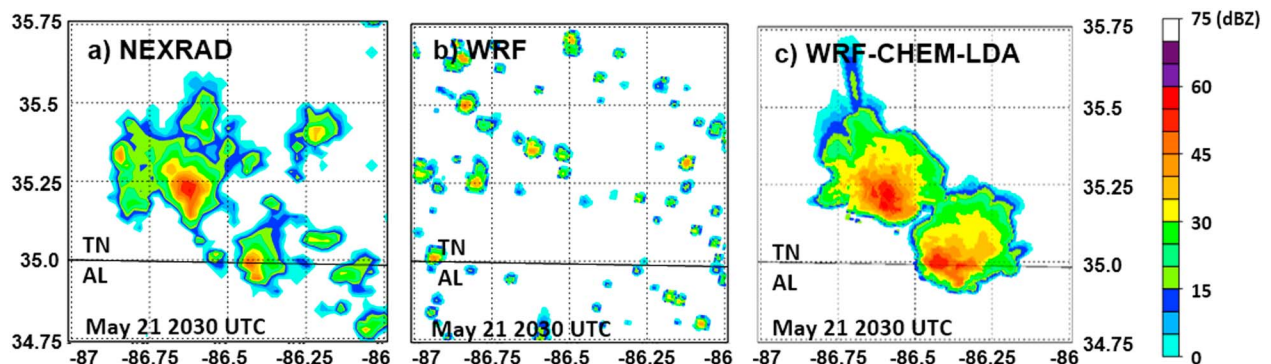


Figure 8. Composite reflectivity at 2030 UTC on 21 May from (a) NEXRAD, (b) WRF simulation without lightning data assimilation, and (c) WRF-Chem simulation with lightning data assimilation.

Table 2. Mean CO and O₃ Mixing Ratios (ppbv) From Aircraft Measurements and WRF-Chem-LDA Simulations

		Upper Levels					
		Low-Level Inflow		Affected by Storm Outflow		Unaffected by Storm Outflow	
		CO	O ₃	CO	O ₃	CO	O ₃
21 May	Aircraft	150.5 (±9.6)	71.4 (±3.0)	100.2 (±4.5)	143.4 (±25.2)	75.1 (±3.4)	214.3 (±7.6)
	WRF-Chem	152.5 (±2.2)	61.8 (±2.3)	94.2 (±6.7)	147.3 (±25.2)	79.7 (±0.4)	213.0 (±14.3)
29 May	Aircraft	132.3 (±3.1)	32.6 (±0.4)	123.1 (±3.6)	80.0 (±4.8)	104.4 (±5.4)	82.2 (±7.0)
	WRF-Chem	136.3 (±0.3)	44.1 (±3.6)	123.2 (±14.2)	84.7 (±12.9)	96.3 (±3.4)	97.1 (±6.4)
11 June	Aircraft	117.5 (±4.3)	33.9 (±3.5)	107.9 (±5.0)	111.1 (±16.0)	72.6 (±3.1)	155.3 (±20.2)
	WRF-Chem	112.0 (±7.8)	45.9 (±4.2)	108.8 (±2.1)	101.4 (±14.4)	69.8 (±0.7)	161.8 (±6.1)

$$\frac{\partial}{\partial t} \int_{\Omega} (\bar{\rho} \phi) \partial \Omega = - \int_{\Omega} \frac{\partial (\bar{\rho} w \phi)}{\partial z} \partial \Omega - \int_{\Gamma} (\bar{\rho} u_n \phi) \partial \Gamma \quad (3)$$

where z is height, Ω is horizontal domain, Γ is spatial boundaries, and u_n is the boundary-normal velocity. The last term on the right is the net flux through the boundaries, which is smaller than the other two terms during deep convection. Thus, during deep convection, the local rate of change of tracer mass is approximately equal and opposite in sign to the vertical flux divergence (VFD) of the tracer mass (the first term on the right), which following the *Skamarock et al.* [2000] formula, is defined as

$$\text{VFD} = \sum \frac{\partial \rho w C_{\text{gas}} \frac{M_{\text{gas}}}{M_{\text{air}}}}{\partial z} dx dy \quad \left(\text{Unit} : \frac{\text{kg} \cdot \text{m}}{\text{m}^3 \cdot \text{s}} \cdot \text{m}^2 = \text{kg m}^{-1} \text{s}^{-1} \right) \quad (4)$$

where C_{gas} is the volume mixing ratio of the trace gas, M_{gas} is the molar mass of trace gas, and M_{air} is the molar mass of air.

Besides the strength of vertical transport, another aspect that remains critical in the study of deep convective transport is the depth of vertical transport, which informs us of the altitude range affected by PBL pollution due to deep convective transport. *Mullendore et al.* [2009] used the level of maximum detrainment (LMD) to represent the depth of vertical transport. LMD is the point at which the vertical flux divergence is most negative and horizontal detrainment is at a maximum. The altitude range where vertical divergence is negative is defined as the “detrainment envelope,” which is the vertical region of horizontal detrainment.

5.2. Upward Vertical Transport at Different Storm Stages

Based on the VFD analysis (section 5.1), the LMD and the detrainment envelope were calculated every 10 min for each case during the aircraft sampling period (Figure 9). During this period, the intensity of the 11 June MCS remained at steady state with a nearly constant altitude for the LMD (Figure 9 bottom). For the 21 May air mass case and the 29 May supercell case, CI, development, and mature stage were simulated during the model analysis period. The results illustrate that in the developing stage, the storm LMD increased in altitude and the depth of the detrainment envelope increased. After the storm matured, the LMD gradually became stable. The mature stage LMD is 11 km for 21 May air mass storm, 12 km for 29 May supercell case, and 13 km for 11 June MCS case.

5.3. Upward Vertical Transport at Storm Mature Stage

Using equation (4), the upward mass vertical flux divergence (VFD) was estimated every 10 min over the whole storm region where composite reflectivity is greater than 0 dBZ. Comparing the VFD for the three cases during the mature stage of each storm (Figure 10a), it was found that the total upward transport is strongest for the 11 June MCS case and weakest for the 21 May air mass storm. This is because the storm area of the 11 June MCS is much larger than the other two cases, and it transports more air over the entire storm region from the lower levels to upper levels.

Overall, the MCS case has the greatest ability to transport trace gases and aerosols from the PBL to the upper troposphere due to its larger size and longer duration. The transport of CO to the UT (above 8 km) for the first hour after the storm becomes mature is 7.2×10^5 kg/h for the air mass case, 4.57×10^6 kg/h for the supercell case, and 1.95×10^7 kg/h for the MCS case. Considering the duration of the system (3 h for the air mass case,

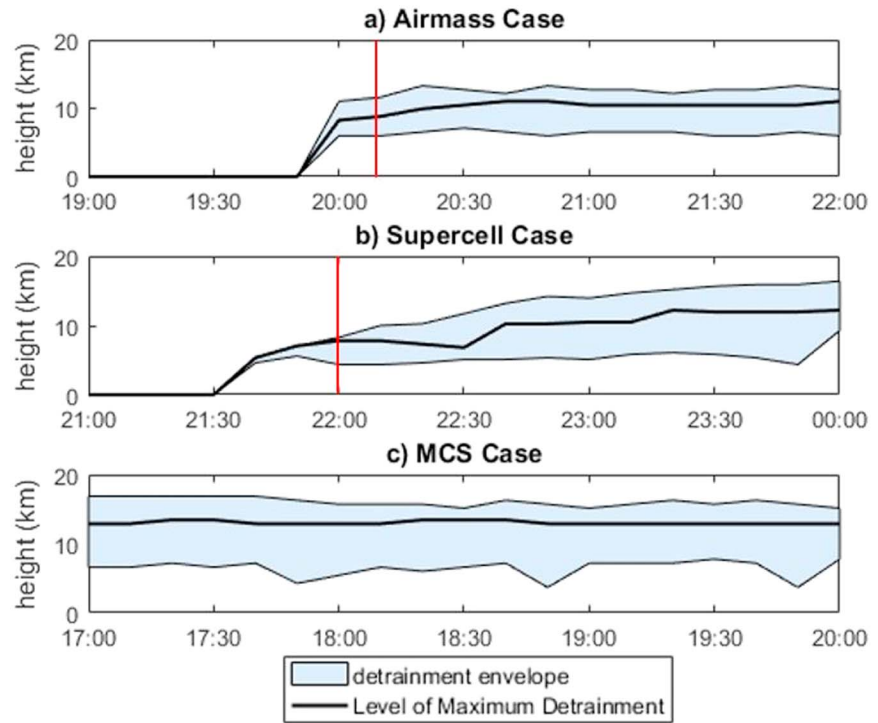


Figure 9. Time series showing WRF-Chem-LDA simulated level of maximum detrainment and detrainment envelope for (a) 21 May air mass storm case, (b) 29 May supercell severe storm case, and (c) 11 June MCS case. The red lines in Figures 9a and 9b represent the time of anvil formation.

6.5 h for the supercell case, and 23 h for the MCS case), the transport of CO in the MCS case may be ~200 times more than the air mass case and 15 times more than the supercell case.

Considering the differences in storm size among the three convective cases, we divided the calculated VFD by the area of the region where there was positive vertical velocity and obtained upward VFD per unit area for each case:

$$\text{VFD per unit area} = \frac{\overline{\partial \rho w C_{\text{gas}} \frac{M_{\text{gas}}}{M_{\text{air}}}}}{\partial z} = \frac{M_{\text{gas}}}{M_{\text{air}}} \left(\overline{\rho w \frac{\partial C_{\text{gas}}}{\partial z}} + C_{\text{gas}} \overline{\frac{\partial \rho w}{\partial z}} \right) \quad (\text{Unit: kg m}^{-3} \text{ s}^{-1}) \quad (5)$$

The upward transport per unit area is strongest for the 29 May case and slightly less for the 11 June MCS and 21 May air mass cases (Figure 10b). In the lower atmosphere, the inflow layer (i.e., the layer with positive vertical flux divergence and, hence, horizontal convergence) extends from the surface to ~6 km altitude, with the most positive values and largest inflow from the surface to 1 km altitude in all three cases. For the 29 May supercell case, the low-level horizontal convergence (positive VFD) layer extends from the surface to ~6 km, which is 1 km deeper than for the 11 June MCS case. Compared to the other cases, the low-level horizontal convergence appears more complex in the 21 May air mass case. The latter exhibits low-level horizontal divergence regions (negative VFD) near 1 km and 3.5 km.

Forward and backward trajectories provide a more in-depth depiction of the inflow and outflow structure. Three dimensional (3-D) renderings of the 3 h trajectories were calculated and plotted by Visualization and Analysis Platform for Ocean, Atmosphere, and Solar Researchers (VAPOR) [Clyne and Rast, 2005; Clyne et al., 2007] using the modeled 3-D wind fields (Figure 11). The horizontal spacing of the trajectories is 3 km for all three cases. The forward trajectories start from 500 m (Figures 11a–11c), 1.5 km (Figures 11d–11f), and 2.5 km (Figures 11g–11i). The initiation times of the forward trajectories are 1900 UTC for the air mass case, 2100 UTC for the supercell case, and 1700 UTC for the MCS case. The backward trajectories (Figures 11j–11l) start from the altitude of the LMD (11 km for the 21 May air mass case, 12 km for the 29 May supercell case, and 13 km for the 11 June MCS case). The initiation time of the

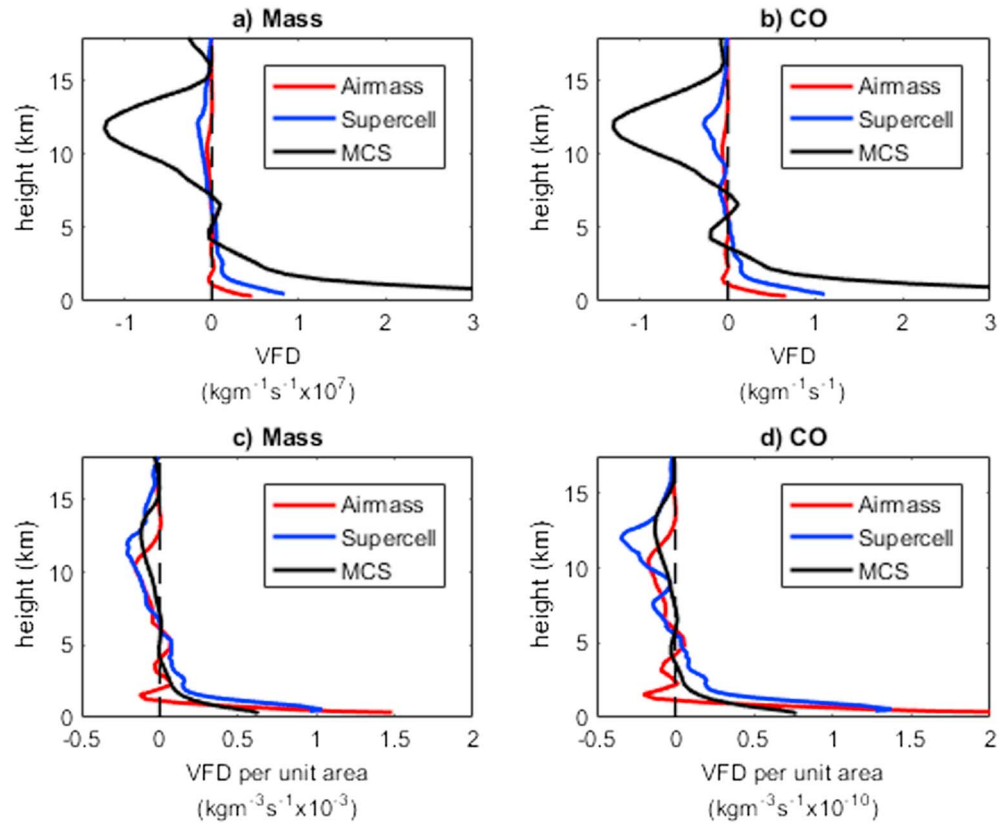


Figure 10. Upward VFD of (a) mass and (b) CO for 21 May air mass storm (red), 29 May supercell storm (blue), and 11 June MCS (black); vertical flux divergence per unit area of (c) mass and (d) CO for the three cases.

backward trajectories are 2200 UTC for the air mass case, 0000 UTC for the supercell case, and 2100 UTC for the MCS case. For the 21 May air mass case, the trajectories indicate that most of the high-level air within the LMD started from above 1.5 km (Figure 11g), while nearly all of the air that originated at 1.5 km or lower (Figures 11a and 11d) remained below 5 km at the end of the 3 h. On the other hand, in the 29 May supercell case (Figures 11b, 11e, and 11h) and the 11 June MCS case (Figures 11c, 11f, and 11i), considerable low-level air was transported to the LMD. Given that the length of the arrows is proportional to the distance traveled in 10 min, air in the supercell and MCS cases can be transported from near the surface to the LMD in less than 30 min.

Following *Mullendore et al.* [2009], we use CO as a tracer to calculate the VFD of trace gas. Results (Figure 10d) show that the upward transport per unit area of CO is the strongest for the 29 May case. Comparing the result of the 29 May supercell case with the *Skamarock et al.* [2000] supercell case, we found that the 3 h time integrated VFD at LMD for the 29 May case is 11 times larger than the supercell case of *Skamarock et al.* [2000], while the size of the 29 May storm system is about 10 times greater. Thus, the VFD per unit area of our supercell case is similar to the results of *Skamarock et al.* [2000].

In order to determine why the vertical flux divergence differs among the three cases, vertical profiles of averaged mass flux density (ρw) and trace gas mixing ratio over the storm region were constructed at the mature stages of each storm and are shown in Figure 12 (see also equation (5)). The mass flux density is largest for the 29 May case. Its large vertical velocity peak reported earlier ($\sim 65 \text{ m s}^{-1}$) contributes to relatively large mass flux density as well as vertical gradient of mass flux density that increases the vertical flux divergence throughout the column. The CO profile for the supercell case has a local maximum at 10 km and a larger vertical gradient than the other cases. This gradient (first term on the right of equation (5)) also contributes to the large CO VFD per unit area on 29 May. Section 5.4 discusses the roles of the vertical gradient of mass flux density and vertical gradient of trace gas mixing ratios in VFD in more detail.

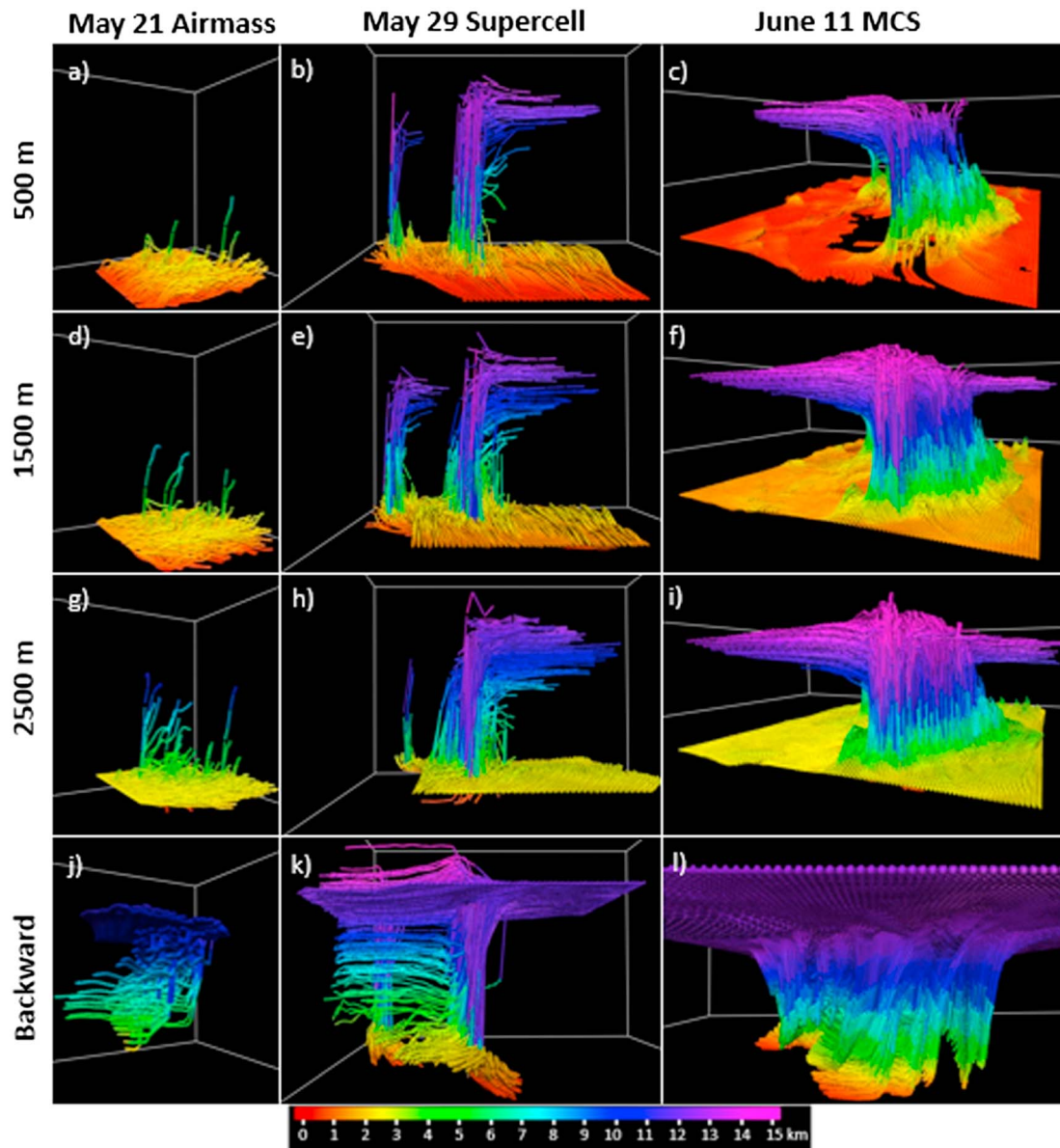


Figure 11. Three-dimensional renderings of 3 h forward trajectories from (a–c) 500 m, (d–f) 1.5 km, (g–i) 2.5 km of the 21 May air mass case (Figures 11a, 11d, and 11g), the 29 May supercell case (Figures 11b, 11e, and 11h), and the 11 June MCS case (Figures 11c, 11f, and 11i), and (j–l) backward trajectories from the LMD of the three cases. Each trajectory line consists of 18 arrows with each arrow representing 10 min air trajectory. The color of the arrows represents the ending height of the trajectories. The horizontal resolution of the trajectory seeds is 5 km for all three cases.

The CO vertical profile is well mixed on 11 June contributing to a relatively low VFD per unit area for this case. In order to understand why the profile is so well mixed on 11 June, we compare CO mixing ratio x-z cross sections for the three cases at six different times (Figures 13–15). The rear side (left side in Figure 15) of the 11 June MCS shows evidence of injection of cleaner mid level air by a rear inflow jet into the lower troposphere, which was not seen in the other two cases. Injection by a rear inflow jet is typical for this type of convection [Houze et al., 1989]. A prominent bow echo occurred during the 11 June MCS event (Figure 5), which was produced by the midlevel strong rear inflow jet. The jet brought relatively clean mid-level air into the storm, which then descended in downdrafts. If this relatively clean air also enters the updraft region, it will reduce the CO mixing ratio vertical gradient, as well as CO mixing ratios in the lower atmosphere. Based on equation (5), decreasing the CO mixing ratio and/or CO mixing ratio vertical gradient will lead to a decrease of vertical flux divergence. In order to test whether the relatively clean air in the rear

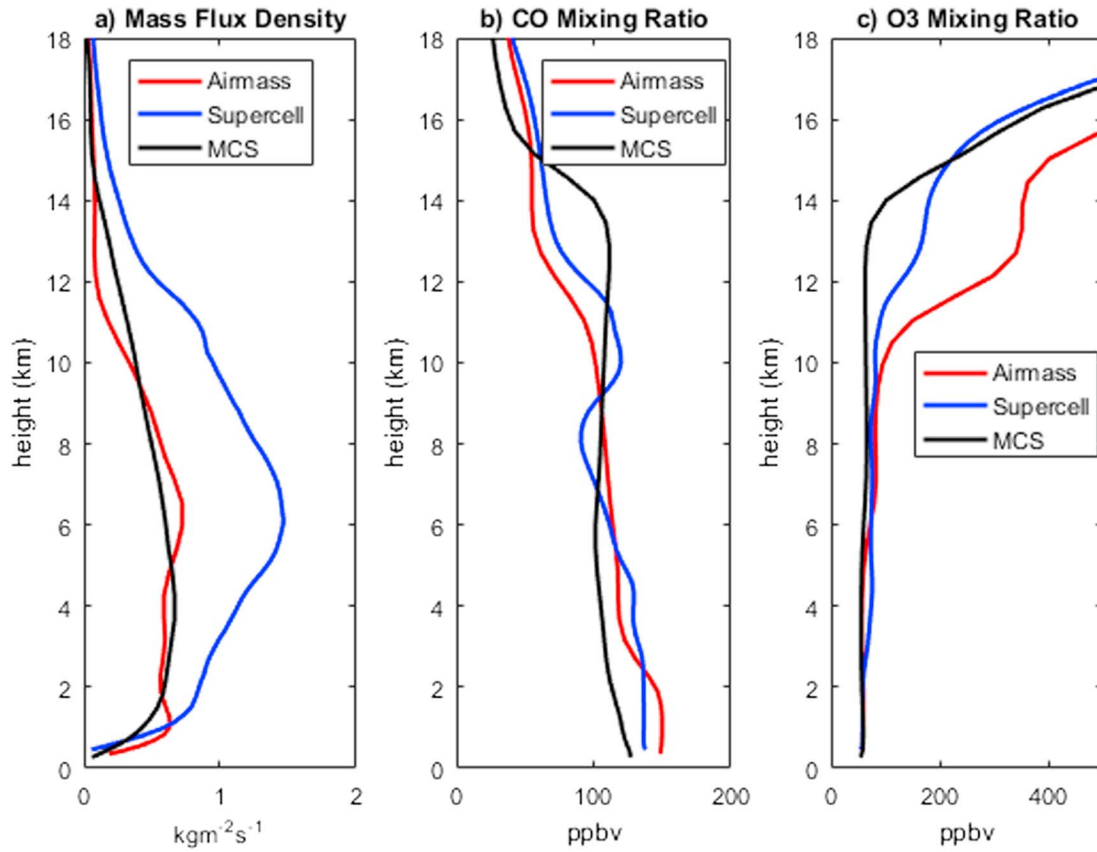


Figure 12. Average (a) mass flux density, (b) CO mixing ratio, and (c) O₃ mixing ratio vertical profiles in the storm region (composite reflectivity >0 dBZ) at the mature stage for the 21 May air mass case (red), the 29 May supercell case (blue), and the 11 June MCS case (black).

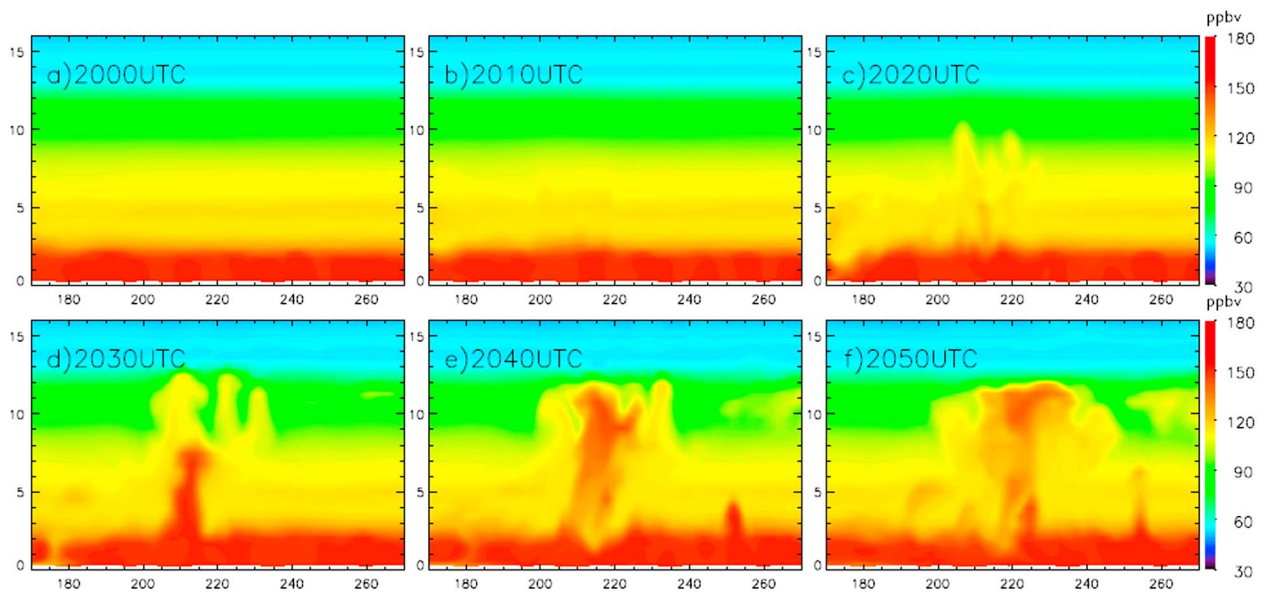


Figure 13. WRF-Chem-LDA simulated CO mixing ratio vertical cross-sections along the black solid line highlighted in Figure 1f, at (a) 2000 UTC, (b) 2010 UTC, (c) 2020 UTC, (d) 2030 UTC, (e) 2040 UTC, and (f) 2050 UTC on 21 May 2012.

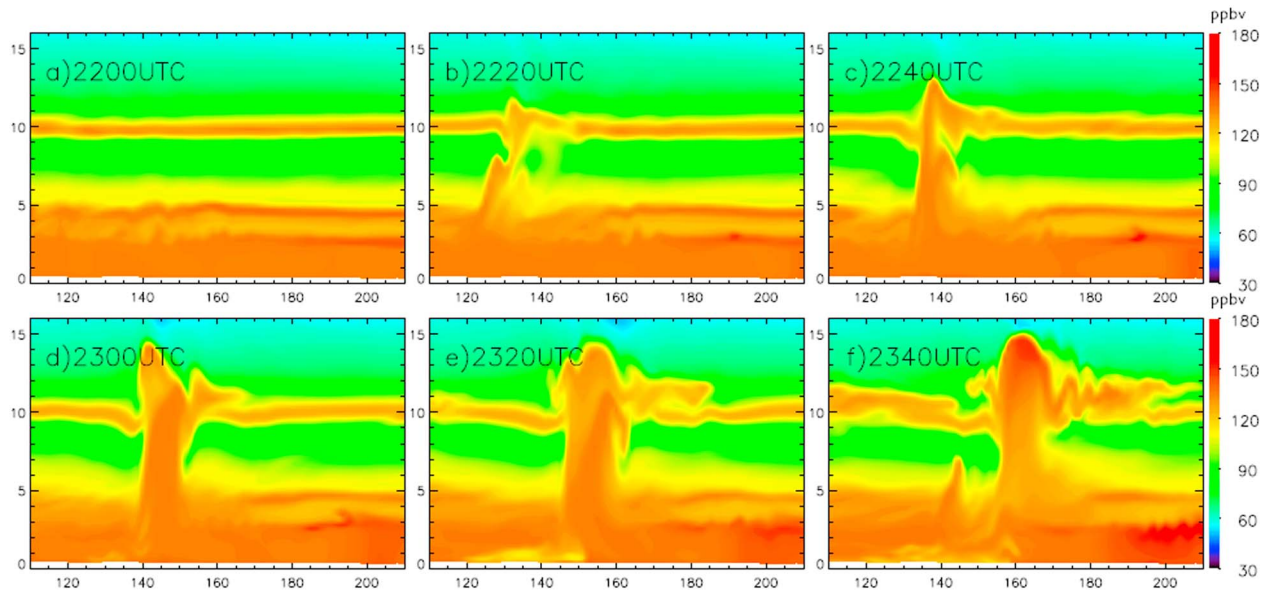


Figure 14. WRF-Chem-LDA simulated CO mixing ratio vertical cross-sections along the black solid line highlighted in Figure 3d, at (a) 2200 UTC, (b) 2220 UTC, (c) 2240 UTC, (d) 2300 UTC, (e) 2320 UTC, and (f) 2340 UTC on 29 May 2012.

side of the storm could enter the storm inflow and be transported to the UT, a tracer experiment was designed to determine the amount of the downdraft air that was transported to the upper levels of the storm. After CI, tracer T was added to the storm downdraft region at one time step and its mixing ratio was evaluated at upper levels of the storm (above 8 km) after 60 min. The mixing ratio for the tracer was set to 0.1 ppmv in the downdraft region from 0 km to 4 km, and 0 elsewhere. After an hour, we calculated the ratio of upper level T mixing ratio and the total mixing ratio of T integrated over the model domain. The tracer calculation was performed for the 21 May and 11 June cases. Here we define the rear inflow ratio as

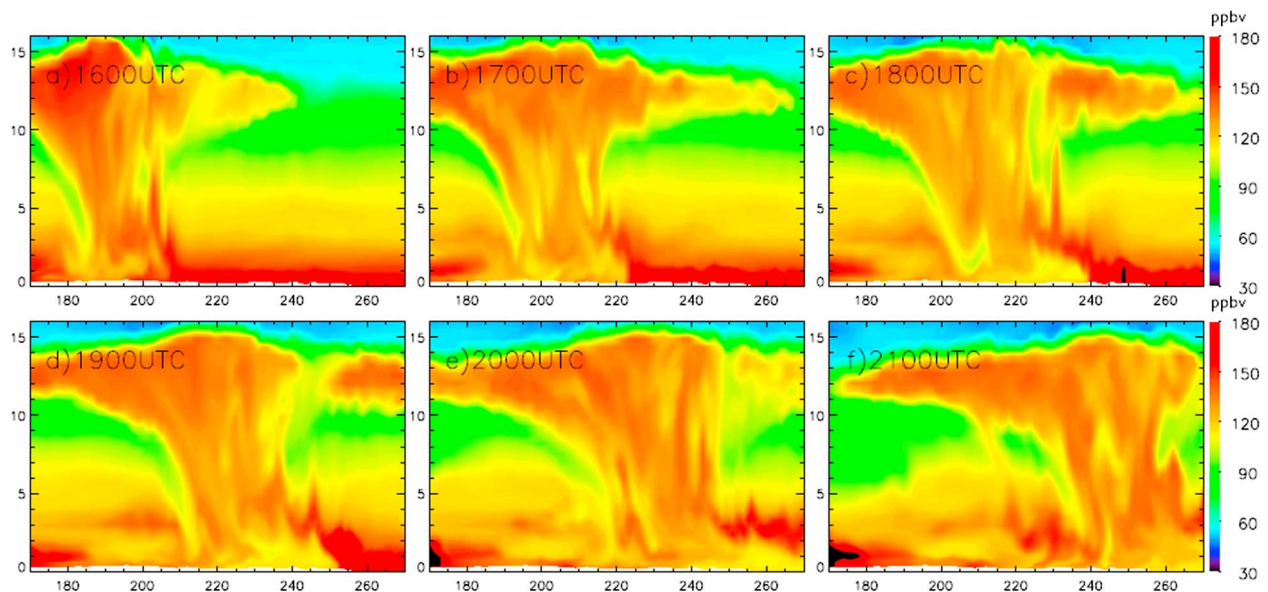


Figure 15. WRF-Chem-LDA simulated CO mixing ratio vertical cross-sections along the black solid line highlighted in Figure 5e at (a) 1600 UTC, (b) 1700 UTC, (c) 1800 UTC, (d) 1900 UTC, (e) 2000 UTC, and (f) 2100 UTC on 11 June 2012.

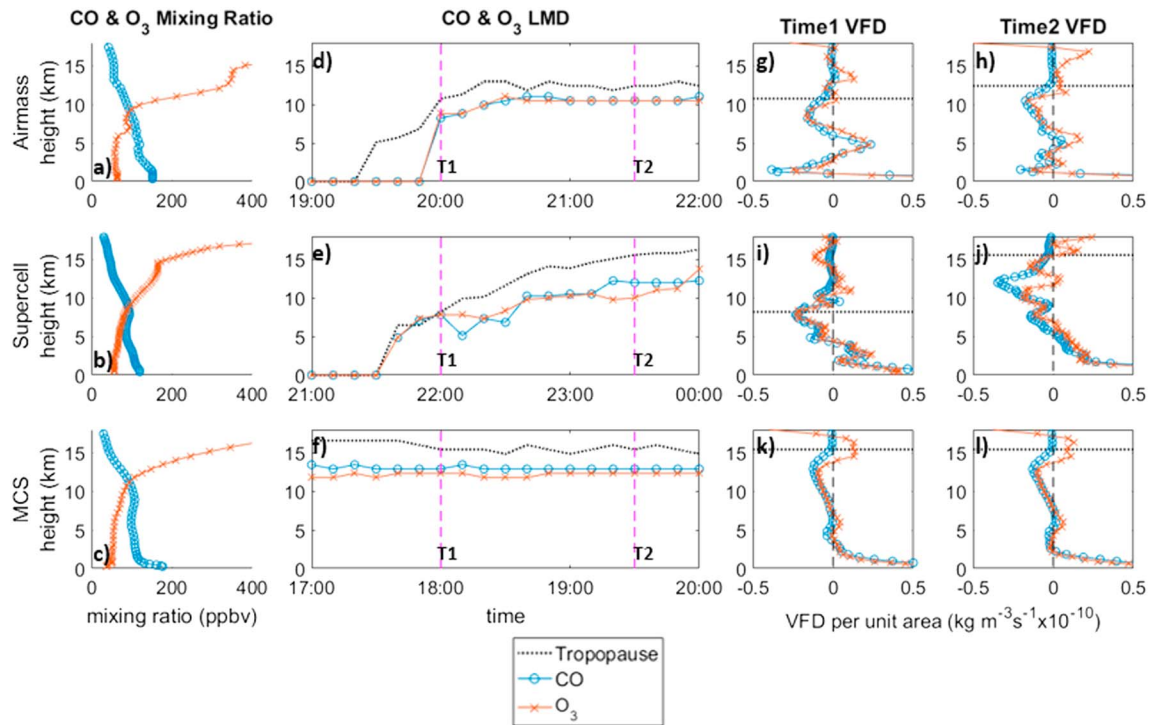


Figure 16. CO (blue) and O₃ (orange) initial mixing ratio vertical profile for (a) 21 May air mass case, (b) 29 May supercell case, and (c) 11 June MCS case. The WRF-Chem-LDA simulated LMD using CO and O₃ as example tracers for (d) 21 May air mass case, (e) 29 May supercell case, and (f) 11 June MCS case. The WRF-Chem-LDA simulated VFD per unit area at Time 1 (T1) and Time 2 (T2) using CO and O₃ as example tracers for (g and h) 21 May air mass case, (i and j) 29 May supercell case, and (k and l) 11 June MCS case are shown. The tropopause (shown by dotted line) is calculated based on the WMO definition.

$$\text{rear inflow ratio} = \frac{\text{high level T mixing ratio}}{\text{total T mixing ratio}} \quad (6)$$

Therefore, the rear inflow ratio increases with the amount of downdraft air entering the updraft. The rear inflow ratio for 21 May is 0.01 after 60 min, while the rear inflow ratio for 11 June is 0.1. Clearly, for the 11 June case, the cleaner downdraft air entered the updraft region. For this case about 10% of the low-level downdraft air was transported to the UT, which leads to the low value of VFD for CO in the upper troposphere.

5.4. Upward Vertical Transport of Different Trace Gases

Different trace gases have different vertical distribution, which might affect the vertical transport pattern (equation (5)). Thus, we choose CO and O₃ as example tracers, which have different and opposite vertical distributions and gradients. Figure 16 shows the initial vertical profiles (Figures 16a–16c), LMD as a function of time (Figures 16d–16f), and VFD (Figures 16g–16l) of CO and O₃. From equation (5), the following is obtained:

$$\text{VFD(per unit area)} \propto \overline{\rho w \frac{\partial C_{\text{gas}}}{\partial z}} + C_{\text{gas}} \frac{\partial \overline{\rho w}}{\partial z} \quad (7)$$

For CO and O₃, the mass flux density (ρw) and its vertical gradient will be the same, while the trace gas vertical gradients will have opposite signs. Therefore, the sign of the first term on the right-hand side will differ between CO and O₃ VFDs, while the second term will have the same sign but different amplitudes. Figure 17 compares the value of the two terms. We call the first term the trace gas gradient term and the second term the mass flux density gradient term, because they control the sign of each term. In the lower troposphere and midtroposphere for all three cases, the mass flux gradient term is much larger than the trace gas gradient term (compare top and bottom rows of Figure 17), which means that to first order the

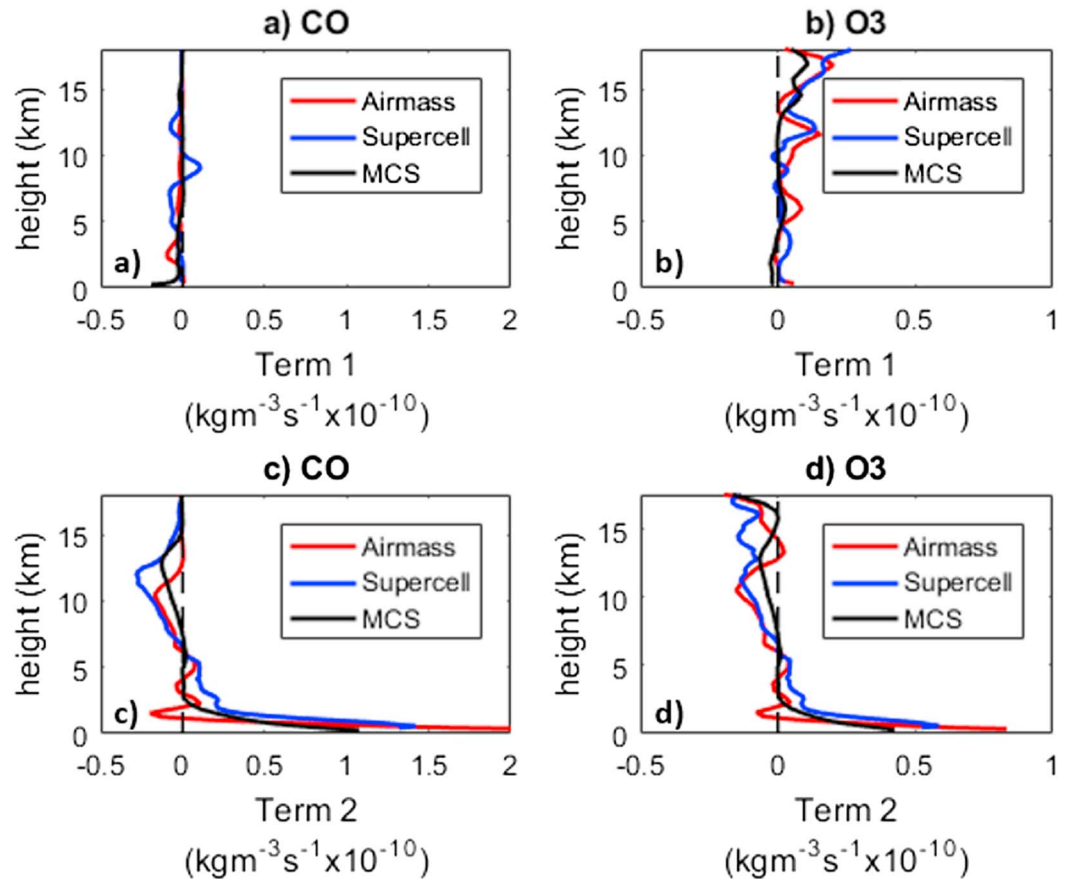


Figure 17. Trace gas gradient terms (the first term on the right side of equation (7)) for CO (a) and O₃ (b) for the 21 May air mass case (red), the 29 May supercell case (blue), and the 11 June MCS case (black). Mass flux density gradient terms (the second term on the right side of equation (7)) for CO (c) and O₃ (d) for same three cases.

product of the trace gas mixing ratio and mass flux gradient controls the VFD distribution, and the direction of the transport is determined by the mass flux gradient rather than the trace gas gradient. This explains why the VFD distributions for CO and O₃ in all three cases are similar (Figures 16g–16l), except in the uppermost troposphere and stratosphere where the trace gas gradient term is important for O₃ due to its strong vertical gradient. In this altitude range, the VFD profiles of O₃ and CO diverge.

5.5. Upward Vertical Transport Compared With Downward Vertical Transport

Besides upward transport, downward transport is also significant. In Figure 18, the VFD of upward transport, downward transport, and total (net) transport are compared side by side. CO vertical transport results show that in the midtroposphere and upper troposphere, net transport has the same sign as upward transport. This means that within this altitude range, upward transport dominates vertical transport. In the lower troposphere, either upward transport or downward transport dominates. The vertical transport for O₃ at high levels remains, however, relatively more complex. Below the cloud top, defined here as the highest altitude where the sum of the mixing ratio of ice, snow, graupel, rain, and cloud exceeds 10⁻³ g kg⁻¹, there is a region where downward O₃ VFD is negative in all three cases. In this region, downward transport of high mixing ratio stratospheric O₃ causes O₃ convergence (negative net O₃ VFD). This model simulation result is similar to the observations. Huntrieser et al. [2016] analyzed the in situ measurement of O₃ and reported that O₃-rich air from the LS was transported downward into the anvil and also surrounded the outflow. Pan et al. [2014] found that the wrapping of O₃-rich stratospheric air around the edge of the storm led to a ram-horn-shaped O₃ enhancement around the cloud edge reaching altitudes as low as 4 km below the local tropopause in the 30 May DC3 MCS case. Above the cloud top,

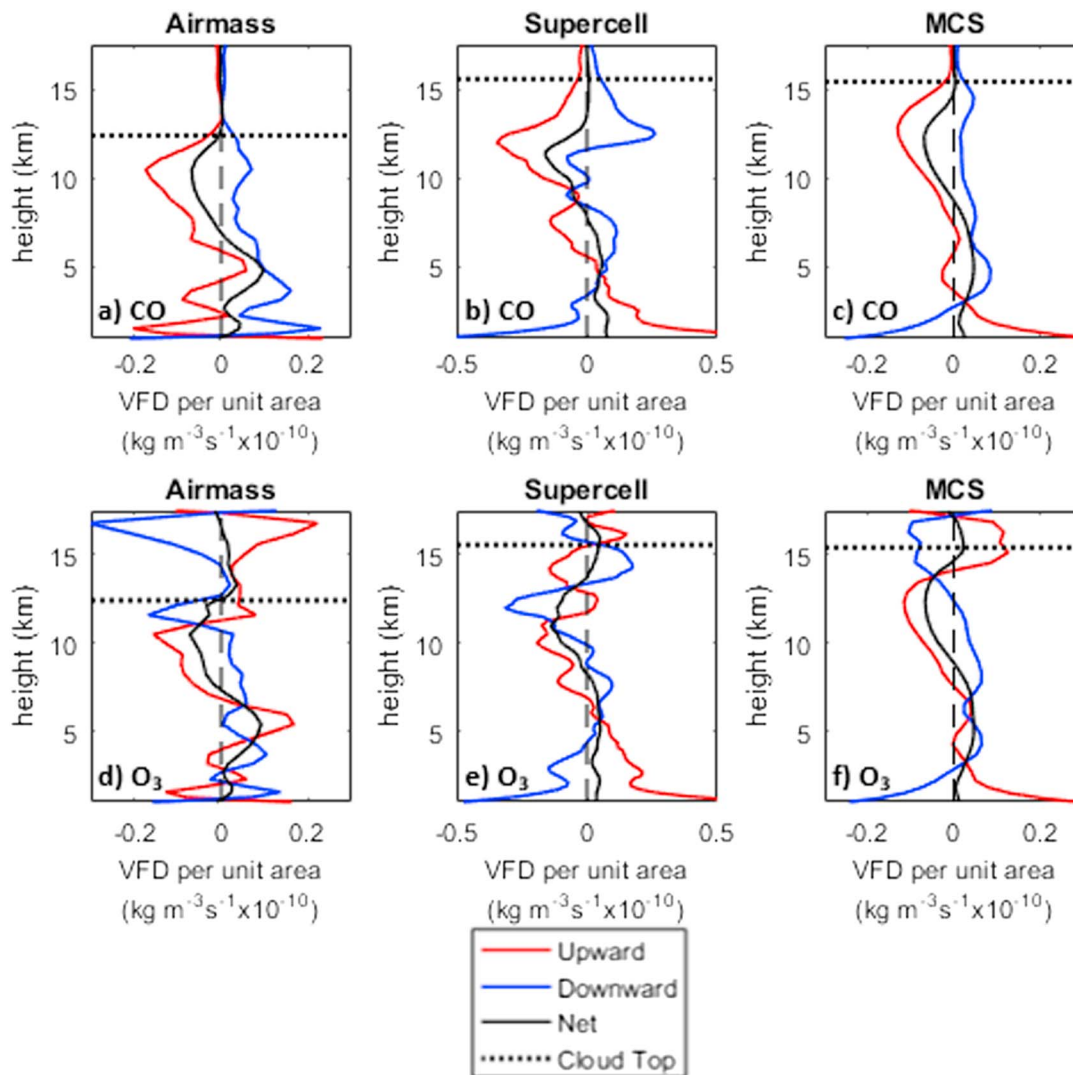


Figure 18. WRF-Chem-LDA simulated upward (red), downward (blue), and net (black) VFD per unit area using (a, b, c) CO and (d, e, f) O₃ as example tracers for the 21 May air mass case, the 29 May supercell case, and the 11 June MCS case.

there is a positive O₃ VFD region. In that region, the O₃ VFD divergence is caused by upward transport of low mixing ratio O₃ to the stratosphere.

5.6. Vertical Transport in Different Composite Reflectivity Regions

Sensitivity tests for vertical transport were simulated for different composite reflectivity regions. For each storm, the VFD per unit area and LMD were calculated every 10 min (Figure 19) within four composite reflectivity regions characterized by reflectivities exceeding 0 dBZ, 20 dBZ, 30 dBZ, and 40 dBZ. During the development stage of the 21 May air mass case and the 29 May supercell case, the heights of LMD vary between reflectivity regions, and the detrainment envelope is narrower in high reflectivity regions than in low reflectivity regions (at most 4 km narrower). After the storm matured, the heights of LMD and the detrainment envelope converge and become similar in all reflectivity regions. For the 11 June MCS case, the height of the LMD is insensitive to reflectivity region and varies little with time. In contrast to the air mass and supercell cases, the detrainment envelope for the MCS case is deeper in high reflectivity regions than in low reflectivity regions. The detrainment envelope for the region >40 dBZ is 2 km thicker than the envelope for the region >0 dBZ. Moreover, VFD analysis reveals that for all three cases, VFD per unit area remains stronger in the region >40 dBZ region (storm core). Based on the analysis for these storm cases, the mean VFD per unit area in the region >40 dBZ can be a factor 2–5 fold larger than the mean VFD in the region >0 dBZ.

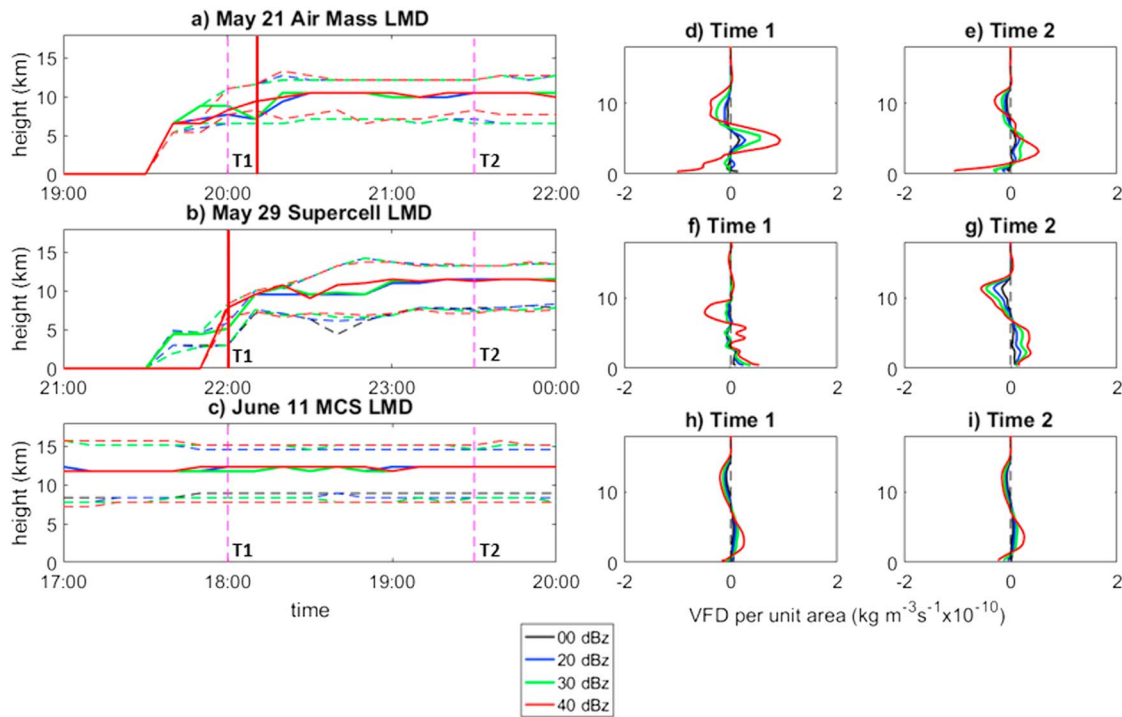


Figure 19. Time series of LMD from WRF-Chem simulations with LDA within four different reflectivity regions (exceeding: 00 dBZ (black), 20 dBZ (blue), 30 dBZ (green), and 40 dBZ (red), respectively) for (a) the 21 May air mass case, (b) the 29 May supercell case, and (c) the 11 June MCS case. The colored dashed lines represent the detrainment envelope of each reflectivity region. WRF-Chem-LDA simulated net VFD per unit area at Time 1 (T1) and Time 2 (T2) within different reflectivity regions for (d and e) the 21 May air mass case, (f and g) the 29 May supercell case, and (h and i) the 11 June MCS case. The vertical red lines in Figures 19a and 19b represent the time of anvil formation.

6. Conclusions

In this study, we analyze the deep convective transport in three different convective regimes from the DC3 field campaign using WRF-Chem simulations. After constraining the model solution via a computationally inexpensive lightning data assimilation technique [Fierro *et al.*, 2012, 2015], the model was able to better reproduce storm location, timing of convection initiation, spatial structure, and hence, the chemical distributions of interest.

The analysis of CO vertical transport demonstrated that the upward vertical flux divergence per unit area of the 29 May severe supercell case was the strongest, while the upward vertical flux divergence per unit area of the areally expansive 11 June MCS case is comparable to that of the smaller 21 May air mass case. This result is in agreement with Bigelbach *et al.* [2014]. For the air mass case, trajectories indicate that nearly all of the air parcels that originated below 1.5 km remained below 5 km, while air within the supercell and MCS systems was transported from near the surface to about 10 km in about 30 min.

Trace gas vertical cross sections were examined, and a tracer transport experiment was conducted to unveil some of the factors behind the simulated weak vertical transport of CO in the MCS case. The analysis revealed that a rear inflow jet transported relatively clean midlevel air into the downdraft region, which then descended and was entrained into the updraft region. This reduced trace gas mixing ratios in the low-level inflow and decreased the vertical gradient of trace gases, which contributed to the low VFD values.

We found that during storm development, the level of maximum detrainment became higher in altitude, and the depth of the detrainment envelope increased. Also, when analyzing two trace gases (CO and O₃) with different vertical profiles, it was found that the vertical flux divergence profiles of the two trace gases looked similar in the lower and mid troposphere, indicating that in this altitude range, the VFD profile is mostly controlled by the vertical distribution of mass flux density as opposed to the vertical distribution of the mixing ratio. In the upper troposphere, however, the CO and O₃ VFD profiles differed owing to strong O₃

gradients present at these levels. Comparing CO upward and downward transport, we found that upward transport dominates the vertical transport in the midtroposphere and upper troposphere. Nevertheless, the downward transport of stratospheric O₃ cannot be ignored. Sensitivity tests for vertical transport in different reflectivity regions show us that vertical transport remains stronger in the higher composite reflectivity region of the storms.

A detailed investigation of deep convective transport in different convective regimes is fundamental to understanding how deep convective transport influences the radiation budget and climate of the Earth. We have examined convective transport for case studies representing three types of convection. Quantifying the relative frequency of different types of convection using data from satellites and other sources is an active area of research [e.g., Machado and Rossow, 1993; Tan et al., 2013; Tselioudis et al., 2013; Cotton et al., 1995]. However, comprehensive studies with detailed storm classification of the global frequencies of different convective regimes are lacking. For example, studies showing detailed classifications of storms (i.e., squall lines with different stratiform rain patterns, bow echo, supercell, multicell, isolated cells, and broken line) are needed. In addition, studies with a detailed classification of convective regimes [e.g., Gallus et al., 2008; Schoen and Ashley, 2010] need to be expanded to include additional regions. Comprehensive studies to determine these frequencies are lacking, but this is recommended as an area of future work. Next, it would be interesting to examine the deep convective transport of other trace gases, water vapor, and aerosol in different convective regimes. Also, it is worthy to evaluate and improve the cumulus parameterized deep convective transport in different convective regimes using cloud-resolved simulations such as presented here.

Acknowledgments

This work was supported under NSF grant AGS-1522551 for analysis and modeling associated with the Deep Convective Clouds and Chemistry (DC3) field campaign. M. Bela was supported by NASA ACCDAM-NNX14AR56G and a National Research Council Research Associateship in the Global Systems Division (GSD) at NOAA-ESRL. We thank the NCAR Computational Systems Laboratory (CISL) for usage of the Yellowstone supercomputer for conducting the storm simulations. We extend our appreciation to Tom Ryerson for the DC8 observations of O₃. We would like to thank C.R. Homeyer who provided us the NEXRAD data for all three cases. Thanks also go out to Christopher Sloop and Stan Heckman for providing the ENTLN total lightning data. We acknowledge use of UAH Mobile Radiosonde Observation Data available at http://data.eol.ucar.edu/datafile/nph-get/353.100/Readme_DC3_UAH_Mobile_soundings.html, upper air data for the Oklahoma region from the NSSL available at <http://data.eol.ucar.edu/codiac/dss/id=353.105>, routine upper air observations from NWS available at <http://data.eol.ucar.edu/codiac/dss/id=353.040>, MOZART-4 global model output available at <http://www.aom.ucar.edu/wrf-chem/mozart.shtml>, FINN biomass burning emission data available at <http://bai.aom.ucar.edu/Data/fire/>, and MEGAN emission factors available at <http://www.aom.ucar.edu/wrf-chem/download.shtml>. We appreciate the discussions with Gretchen Mullendore on this work. WRF-Chem model output is available upon request to Yunyao Li (liyuyao@terpmail.umd.edu).

References

- Apel, E. C., et al. (2015), Upper tropospheric ozone production from lightning NO_x-impacted convection: Smoke ingestion case study from the DC3 campaign, *J. Geophys. Res. Atmos.*, *120*, 2505–2523, doi:10.1002/2014JD022121.
- Barth, M. C., et al. (2007), Cloud-scale model intercomparison of chemical constituent transport in deep convection, *Atmos. Chem. Phys.*, *7*, 4709–4731.
- Barth, M. C., J. Lee, A. Hodzic, G. Pfister, W. C. Skamarock, J. Worden, J. Wong, and D. Noone (2012), Thunderstorms and upper troposphere chemistry during the early stages of the 2006 North American Monsoon, *Atmos. Chem. Phys.*, *12*, 11,003–11,026.
- Barth, M. C., et al. (2015), The Deep Convective Clouds and Chemistry (DC3) field campaign, *Bull. Am. Meteorol. Soc.*, *96*, 1281–1309.
- Baughcum, S., et al. (1999), Aircraft emissions: Current inventories and future scenarios. Scholarship at Penn Libraries.
- Bela, M. M., et al. (2016), Wet scavenging of soluble gases in DC3 deep convective storms using WRF-Chem simulations and aircraft observations, *J. Geophys. Res. Atmos.*, *121*, 4233–4257, doi:10.1002/2015JD024623.
- Bertram, T. H., et al. (2007), Direct measurements of the convective recycling of the upper troposphere, *Science*, *315*, 816–820.
- Bigelbach, B. C., G. L. Mullendore, and M. Starzec (2014), Differences in deep convective transport characteristics between quasi-isolated strong convection and mesoscale convective systems using seasonal WRF simulations, *J. Geophys. Res. Atmos.*, *119*, 11,445–11,455, doi:10.1002/2014JD021875.
- Biggerstaff, M. I., L. J. Wicker, J. Guynes, C. Ziegler, J. M. Straka, E. N. Rasmussen, A. Dogget IV, L. D. Carey, J. L. Schroeder, and C. Weiss (2005), The Shared Mobile Atmospheric Research and Teaching (SMART) radar: A collaboration to enhance research and teaching, *Bull. Am. Meteorol. Soc.*, *86*, 1263–1274, doi:10.1175/BAMS-86-9-1263.
- Chen, G., Langley Research Center (LaRC), NASA, and J. Olson (2014a), NSF/NCAR GV HIAPER 1 Minute Data Merge. Version 1.0. UCAR/NCAR - Earth Observing Laboratory. [Available <https://data.eol.ucar.edu/dataset/353.196>.]
- Chen, G., Langley Research Center (LaRC), NASA, and J. Olson (2014b), NSF/NCAR GV HIAPER 1 Second Data Merge. Version 1.0. UCAR/NCAR - Earth Observing Laboratory. [Available <https://data.eol.ucar.edu/dataset/353.194>.]
- Chen, G., Langley Research Center (LaRC), NASA, and J. Olson (2016a), NASA DC-8 1 Minute Data Merge, Version 4.0. UCAR/NCAR - Earth Observing Laboratory. [Available at <http://data.eol.ucar.edu/dataset/353.192>.]
- Chen, G., Langley Research Center (LaRC), NASA, and J. Olson (2016b), NASA DC-8 1 Second Data Merge, Version 4.0. UCAR/NCAR - Earth Observing Laboratory. [Available at <http://data.eol.ucar.edu/dataset/353.189>.]
- Chin, M., P. Ginoux, S. Kinne, O. Torres, B. N. Holben, B. N. Duncan, R. V. Martin, J. A. Logan, A. Higurashi, and T. Nakajima (2002), Tropospheric aerosol optical thickness from the GOCART model and comparisons with Satellite and Sun photometer measurements, *J. Atmos. Sci.*, *59*, 461–483.
- Clyne, J., and M. Rast (2005), A prototype discovery environment for analyzing and visualizing terascale turbulent fluid flow simulations, in *Visualization and Data Analysis 2005*, edited by R. F. Erbacher et al., pp. 284–294, SPIE, Bellingham, Wash. [Available at <http://www.vapor.ucar.edu>.]
- Clyne, J., P. Mininni, A. Norton, and M. Rast (2007), Interactive desktop analysis of high resolution simulations: Application to turbulent plume dynamics and current sheet formation, *New J. Phys.*, *9*, 301.
- Cotton, W. R., G. D. Alexander, R. Hertenstein, R. L. Walko, R. L. McAnelly, and M. Nicholls (1995), Cloud venting-A review and some new global annual estimates, *Earth Sci. Rev.*, *39*, 169–206.
- DeCaria, A. J., K. E. Pickering, G. L. Stenchikov, and L. E. Ott (2005), Lightning-generated NO_x and its impact on tropospheric ozone production: A three-dimensional modeling study of a Stratosphere-Troposphere Experiment: Radiation, Aerosols and Ozone (STERAO-A) thunderstorm, *J. Geophys. Res.*, *110*, D14303, doi:10.1029/2004JD005556.
- Dickerson, R. R., et al. (1987), Thunderstorms: An important mechanism in the transport of air pollutants, *Science*, *235*, 460–465.
- DiGangi, E. A., D. R. MacGorman, C. L. Ziegler, D. Betten, M. Biggerstaff, M. Bowlan, and C. Potvin (2016), An overview of the 29 May 2012 Kingfisher supercell during DC3, *J. Geophys. Res. Atmos.*, *121*, 14,316–14,343, doi:10.1002/2016JD025690.

- Doswell, C. A., III (2001), Severe convective storms—An overview, in *Severe Convective Storms*, edited by C. A. Doswell III, pp. 1–26, American Meteorological Society, Boston, Mass.
- Emmons, L. K., et al. (2010), Description and evaluation of the Model for Ozone and Related chemical Tracers, version 4 (MOZART-4), *Geosci. Model Dev.*, *3*, 43–67.
- Fast, J. D., W. I. Gustafson, R. C. Easter, R. A. Zaveri, J. C. Barnard, E. G. Chapman, G. A. Grell, and S. E. Peckham (2006), Evolution of ozone, particulates, and aerosol direct radiative forcing in the vicinity of Houston using a fully coupled meteorology-chemistry-aerosol model, *J. Geophys. Res.*, *111*, D21305, doi:10.1029/2005JD006721.
- Fierro, A. O., E. R. Mansell, C. L. Ziegler, and D. R. MacGorman (2012), Application of a lightning data assimilation technique in the WRF-ARW model at cloud-resolving scales for the tornado outbreak of 24 May 2011, *Mon. Weather Rev.*, *140*, 2609–2627.
- Fierro, A. O., J. Gao, C. L. Ziegler, E. R. Mansell, D. R. MacGorman, and S. R. Dembek (2014), Evaluation of a cloud-scale lightning data assimilation technique and a 3DVAR method for the analysis and short-term forecast of the 29 June 2012 Derecho event, *Mon. Weather Rev.*, *142*, 183–202.
- Fierro, A. O., A. J. Clark, E. R. Mansell, D. R. MacGorman, S. R. Dembek, and C. L. Ziegler (2015), Impact of storm-scale lightning data assimilation on WRF-ARW precipitation forecasts during the 2013 warm season over the contiguous United States, *Mon. Weather Rev.*, *143*, 757–777.
- Fierro, A. O., J. Gao, C. L. Ziegler, K. M. Calhoun, E. R. Mansell, and D. R. MacGorman (2016), Assimilation of flash extent data in the variational framework at convection-allowing scales: Proof-of-concept and evaluation for the short-term Forecast of the 24 May 2011 tornado outbreak, *Mon. Weather Rev.*, *144*, 4373–4393.
- Fried, A., et al. (2016), Convective transport of formaldehyde to the upper troposphere and lower stratosphere and associated scavenging in thunderstorms over the central United States during the 2012 DC3 study, *J. Geophys. Res. Atmos.*, *121*, 7430–7460, doi:10.1002/2015JD024477.
- Gallus, W. A., N. A. Snook, and E. V. Johnson (2008), Spring and summer severe weather reports over the Midwest as a function of convective mode: A preliminary study, *Weather Forecasting*, *23*, 101–113.
- Grell, G. A. (1993), Prognostic evaluation of assumptions used by cumulus parameterizations, *Mon. Weather Rev.*, *121*, 764–787.
- Grell, G. A., and D. Devenyi (2002), A generalized approach to parameterizing convection combining ensemble and data assimilation techniques, *Geophys. Res. Lett.*, *29*(14), 1693, doi:10.1029/2002GL015311.
- Grell, G. A., S. E. Peckham, R. Schmitz, S. A. McKeen, G. Frost, W. C. Skamarock, and B. Eder (2005), Fully coupled “online” chemistry within the WRF model, *Atmos. Environ.*, *39*, 6957–6975.
- Guenther, A., T. Karl, P. Harley, C. Wiedinmyer, P. I. Palmer, and C. Geron (2006), Estimates of global terrestrial isoprene emissions using MEGAN (Model of Emissions of Gases and Aerosols from Nature), *Atmos. Chem. Phys.*, *6*, 3181–3210.
- Halland, J. J., H. E. Fuelberg, K. E. Pickering, and M. Luo (2009), Identifying convective transport of carbon monoxide by comparing remotely sensed observations from TES with cloud modeling simulations, *Atmos. Chem. Phys.*, *9*, 4279–4294.
- Hill, J. D., J. Pilkey, M. A. Uman, D. M. Jordan, W. Rison, P. R. Krehbiel, M. I. Biggerstaff, P. Hyland, and R. Blakeslee (2013), Correlated lightning mapping array and radar observations of the initial stages of three sequentially triggered Florida lightning discharges, *J. Geophys. Res. Atmos.*, *118*, 8460–8481, doi:10.1002/jgrd.50660.
- Homeyer, C. R., et al. (2014), Convective transport of water vapor into the lower stratosphere observed during double-tropopause events, *J. Geophys. Res. Atmos.*, *119*, 10,941–10,958, doi:10.1002/2014JD021485.
- Hong, S.-Y., and J.-O. J. Lim (2006), The WRF single-moment microphysics scheme (WSM6), *J. Korean Meteorol. Soc.*, *42*, 129–151.
- Hong, S.-Y., Y. Noh, and J. Dudhia (2006), A new vertical diffusion package with an explicit treatment of entrainment processes, *Mon. Weather Rev.*, *134*, 2318–2341.
- Houze, R. A., S. A. Rutledge, M. I. Biggerstaff, and B. F. Smull (1989), Interpretation of Doppler weather radar displays of midlatitude mesoscale convective systems, *Bull. Am. Meteorol. Soc.*, *70*, 608–619.
- Huntrieser, H., et al. (2016), On the origin of pronounced O₃ gradients in the thunderstorm outflow region during DC3, *J. Geophys. Res. Atmos.*, *121*, 6600–6637, doi:10.1002/2015JD024279.
- Iacono, M. J., J. S. Delamere, E. J. Mlawer, M. W. Shephard, S. A. Clough, and W. D. Collins (2008), Radiative forcing by long-lived greenhouse gases: Calculations with the AER radiative transfer models, *J. Geophys. Res.*, *113*, D13103, doi:10.1029/2008JD009944.
- Jensen, E. J., L. Pfister, R. Ueyama, J. W. Bergman, and D. Kinnison (2015), Investigation of the transport processes controlling the geographic distribution of carbon monoxide at the tropical tropopause, *J. Geophys. Res. Atmos.*, *120*, 2067–2086, doi:10.1002/2014JD022661.
- Jung, E., Y. Shao, and T. Sakai (2005), A study on the effects of convective transport on regional-scale Asian dust storms in 2002, *J. Geophys. Res.*, *110*, D20201, doi:10.1029/2005JD005808.
- Koren, V., J. Schaake, K. Mitchell, Q.-Y. Duan, F. Chen and J. M. Baker (1999), A parameterization of snowpack and frozen ground intended for NCEP weather and climate models, *J. Geophys. Res.*, *104*(D16), 19,569–19,585, doi:10.1029/1999JD900232.
- Levizzani, V., and M. Setvák (1996), Multispectral, high-resolution satellite observations of plumes on top of convective storms, *J. Atmos. Sci.*, *53*, 361–369.
- Livesey, N. J., J. A. Logan, M. L. Santee, J. W. Waters, R. M. Doherty, W. G. Read, L. Froidevaux, and J. H. Jiang (2013), Interrelated variations of O₃, CO and deep convection in the tropical/subtropical upper troposphere observed by the Aura Microwave Limb Sounder (MLS) during 2004–2011, *Atmos. Chem. Phys.*, *13*, 579–598.
- Machado, L. A. T., and W. B. Rossow (1993), Structural Characteristics and Radiative Properties of Tropical Cloud Clusters, *Mon. Weather Rev.*, *121*, 3234–3260.
- Marchand, M. R., and H. E. Fuelberg (2014), Assimilation of lightning data using a nudging method involving low-level warming, *Mon. Weather Rev.*, *142*, 4850–4871.
- Mecikalski, R. M., A. L. Bain, and L. D. Carey (2015), Radar and lightning observations of deep moist convection across northern Alabama during DC3: 21 May 2012, *Mon. Weather Rev.*, *143*, 2774–2794.
- Morrison, H., G. Thompson, and V. Tatarskii (2009), Impact of cloud microphysics on the development of trailing Stratiform precipitation in a simulated squall line: comparison of one- and two-moment schemes, *Mon. Weather Rev.*, *137*, 991–1007.
- Mullendore, G. L., D. R. Durran, and J. R. Holton (2005), Cross-tropopause tracer transport in midlatitude convection, *J. Geophys. Res.*, *110*, D06113, doi:10.1029/2004JD005059.
- Mullendore, G. L., A. J. Homann, K. Bevers, and C. Schumacher (2009), Radar reflectivity as a proxy for convective mass transport, *J. Geophys. Res.*, *114*, D16103, doi:10.1029/2008JD011431.
- Pan, L. L., et al. (2014), Thunderstorms enhance tropospheric ozone by wrapping and shedding stratospheric air, *Geophys. Res. Lett.*, *41*, 7785–7790, doi:10.1002/2014GL061921.
- Peckham, S., et al. (2011), WRF-Chem version 3.3 user’s guide, NOAA Tech. Memo., 98 pp.

- Petersen, W. A., et al. (2005), The UAH-NSSTC/WHNT ARMOR C-band dual-polarimetric radar: A unique collaboration in research, education and technology transfer, 32nd Conf. on Radar Meteorology, Preprints, Amer. Meteor. Soc., Albuquerque, N. M.
- Pickering, K. E., R. R. Dickerson, G. J. Huffman, J. F. Boatman, and A. Schanot (1988), Trace gas transport in the vicinity of frontal convective clouds, *J. Geophys. Res.*, *93*, 759–773, doi:10.1029/JD093iD01p00759.
- Pickering, K. E., R. R. Dickerson, W. T. Luke, and L. J. Nunnermacker (1989), Clear-sky vertical profiles of trace gases as influenced by upstream convective activity, *J. Geophys. Res.*, *94*, 14,879–14,892, doi:10.1029/JD094iD12p14879.
- Pickering, K. E., A. M. Thompson, R. R. Dickerson, W. T. Luke, D. P. McNamara, J. P. Greenberg, and P. R. Zimmerman (1990), Model calculations of tropospheric ozone production potential following observed convective events, *J. Geophys. Res.*, *95*, 14,049–14,062.
- Pickering, K. E., A. M. Thompson, J. R. Scala, W.-K. Tao, J. Simpson, and M. Garstang (1991), Photochemical ozone production in tropical squall line convection during NASA Global Tropospheric Experiment/Amazon Boundary Layer Experiment 2A, *J. Geophys. Res.*, *96*, 3099–3114, doi:10.1029/90JD02284.
- Pickering, K. E., J. R. Scala, A. M. Thompson, W.-K. Tao, and J. Simpson (1992a), A regional estimate of convective transport of CO from biomass burning, *Geophys. Res. Lett.*, *19*, 289–292, doi:10.1029/92GL00036.
- Pickering, K. E., A. M. Thompson, J. R. Scala, W.-K. Tao, and J. Simpson (1992b), Ozone production potential following convective redistribution of biomass burning emissions, *J. Atmos. Chem.*, *14*, 297–313.
- Pickering, K. E., A. M. Thompson, J. R. Scala, W.-K. Tao, R. R. Dickerson, and J. Simpson (1992c), Free tropospheric ozone production following entrainment of urban plumes into deep convection, *J. Geophys. Res.*, *97*, 17,985–18,000, doi:10.1029/92JD01716.
- Pickering, K. E., et al. (1996), Convective transport of biomass burning emissions over Brazil during TRACE a, *J. Geophys. Res.*, *101*, 23,993–24,012, doi:10.1029/96JD00346.
- Pickering, K. E., et al. (2001), Trace gas transport and scavenging in PEM-Tropics B South Pacific Convergence Zone convection, *J. Geophys. Res.*, *106*, 32,591–32,607.
- Price, C., and D. Rind (1992), A simple lightning parameterization for calculating global lightning distributions, *J. Geophys. Res.*, *97*(D9), 9919–9933, doi:10.1029/92JD00719.
- Sakulyanontvittaya, T., T. Duhl, C. Wiedinmyer, D. Helmig, S. Matsunaga, M. Potosnak, J. Milford, and A. Guenther (2008), Monoterpene and sesquiterpene emission estimates for the United States, *Environ. Sci. Technol.*, *42*, 1623–1629.
- Scala, J. R., et al. (1990), Cloud draft structure and trace gas transport, *J. Geophys. Res.*, *95*, 17,015–17,030, doi:10.1029/JD095iD10p17015.
- Schoen, J. M., and W. S. Ashley (2010), A climatology of fatal convective wind events by storm type, *Weather Forecasting*, *26*, 109–121.
- Setvák, M., and C. A. Doswell III (1991), The AVHRR Channel 3 cloud top reflectivity of convective storms, *Mon. Weather Rev.*, *119*, 841–847.
- Siu, L. W., K. P. Bowman, and C. C. Epifanio (2015), Convective transport of trace species observed during the stratosphere-troposphere analyses of regional transport 2008 experiment, *J. Geophys. Res. Atmos.*, *120*, 10,530–10,547, doi:10.1002/2015JD023645.
- Skamarock, W. C., and J. B. Klemp (2008), A time-split nonhydrostatic atmospheric model for weather research and forecasting applications, *J. Comput. Phys.*, *227*, 3465–3485.
- Skamarock, W. C., J. G. Powers, M. Barth, J. E. Dye, T. Matejka, D. Bartels, K. Baumann, J. Stith, D. D. Parrish, and G. Hubler (2000), Numerical simulations of the July 10 stratospheric-tropospheric experiment: Radiation, aerosols, and ozone/deep convection experiment convective system: Kinematics and transport, *J. Geophys. Res.*, *105*, 19,973–19,990, doi:10.1029/2000JD900179.
- Solomon, S., K. H. Rosenlof, R. W. Portmann, J. S. Daniel, S. M. Davis, T. J. Sanford, and G.-K. Plattner (2010), Contributions of stratospheric water vapor to decadal changes in the rate of global warming, *Science*, *327*, 1219–1223.
- Stenchikov, G., R. Dickerson, K. Pickering, W. Ellis, B. Doddridge, S. Kondragunta, O. Poulida, J. Scala, and W.-K. Tao (1996), Stratosphere-troposphere exchange in a midlatitude mesoscale convective complex: 2. Numerical simulations, *J. Geophys. Res.*, *101*, 6837–6851.
- Sukoriansky, S., B. Galperin, and V. Perov (2005), Application of a new spectral theory of stably stratified turbulence to the atmospheric boundary layer over sea ice, *Boundary Layer Meteorol.*, *117*, 231–257.
- Tan, J., C. Jakob, and T. P. Lane (2013), On the identification of the large-scale properties of tropical convection using cloud regimes, *J. Clim.*, *26*, 6618–6632.
- Tewari, M., F. Chen, W. Wang, J. Dudhia, M. A. LeMone, K. Mitchell, M. Ek, G. Gayno, J. Wegiel, and R. H. Cuenca (2004), Implementation and verification of the unified NOAA land surface model in the WRF model, in *Proceedings of 20th Conference on Weather Analysis and Forecasting/16th Conference on Numerical Weather Prediction*, pp. 11–15, Seattle, Wash.
- Thompson, A. M., K. E. Pickering, R. R. Dickerson, W. G. Ellis, D. J. Jacob, J. R. Scala, W.-K. Tao, D. P. McNamara, and J. Simpson (1994), Convective transport over the central United States and its role in regional CO and ozone budgets, *J. Geophys. Res.*, *99*, 18,703–18,711, doi:10.1029/94JD01244.
- Tie, X., S. Madronich, S. Walters, R. Zhang, P. Rasch, and W. Collins (2003), Effect of clouds on photolysis and oxidants in the troposphere, *J. Geophys. Res.*, *108*(D20), 4642, doi:10.1029/2003JD003659.
- Tselioudis, G., W. Rossow, Y. Zhang, and D. Konsta (2013), Global weather states and their properties from passive and active satellite cloud retrievals, *J. Clim.*, *26*, 7734–7746.
- Wang, Y., W.-K. Tao, K. E. Pickering, A. M. Thompson, J. S. Kain, R. F. Adler, J. Simpson, P. R. Keehn, and G. S. Lai (1996), Mesoscale model simulations of TRACE A and preliminary regional experiment for storm-scale operational and research meteorology convective systems and associated tracer transport, *J. Geophys. Res.*, *101*, 24,013–24,027, doi:10.1029/96JD00933.
- Wiedinmyer, C., S. K. Akagi, R. J. Yokelson, L. K. Emmons, J. A. Al-Saadi, J. J. Orlando, and A. J. Soja (2011), The Fire INventory from NCAR (FINN): A high resolution global model to estimate the emissions from open burning, *Geosci. Model Dev.*, *4*, 625–641, doi:10.5194/gmd-4-625-2011.